EXPERIMENTAL INVESTIGATION OF DRAG REDUCTION BY TRAILING EDGE TABS ON A SQUARE BASED BLUFF BODY IN GROUND EFFECT

A Thesis

presented to

the Faculty of California Polytechnic State University,

San Luis Obispo

In Partial Fulfillment

of the Requirements for the Degree

Master of Science in Aerospace Engineering

by

Scott Randall Sawyer

May 2015

COMMITTEE MEMBERSHIP

TITLE:	Experimental Investigation of Drag Reduction by Trailing Edge Tabs on a Square Based Bluff Body in Ground Effect
AUTHOR:	Scott Randall Sawyer
DATE SUBMITTED:	May 2015
COMMITTEE CHAIR:	Faysal Kolkailah, Ph.D. Professor of Aerospace Engineering
COMMITTEE MEMBER:	Jin Tso, Ph.D. Professor of Aerospace Engineering
COMMITTEE MEMBER:	Dianne DeTurris, Ph.D. Professor of Aerospace Engineering
COMMITTEE MEMBER:	Russell Westphal, Ph.D. Professor of Mechanical Engineering

ABSTRACT

Experimental Investigation of Drag Reduction by Trailing Edge Tabs on a Square Based Bluff Body in Ground Effect

Scott Randall Sawyer

This thesis presents an experimental investigation of drag reduction devices on a bluff body in ground effect. It has previously been shown that the addition of end-plate tabs to a rectangular based bluff body with an aspect ratio of 4 is effective in eliminating vortex shedding and reducing drag for low Reynolds number flows. In the present study a square based bluff body, both with and without tabs, will be tested under the same conditions, except this time operating within proximity to a ground plane in order to mimic the properties of bounded aerodynamics that would be present for a body in ground effect. The testing was done in the Cal Poly 3ft by 4ft wind tunnel, and was conducted in two phases.

The first phase was base pressure measurements on the body with no tabs. Pressure readings were achieved via thirty pressure ports that were tapped into the base of the model, allowing for fifteen pressure readings in each of the spanwise and normal directions. Baseline data was taken with no ground plane installed in the wind tunnel, mimicking an unbounded flow case and creating a baseline against which further data could be compared once the ground plane was introduced. Three tests were then performed with the ground plane 12.7, 6.35, 3.175 cm (5, 2.5, and 1.25 inches) away, corresponding to values of 1h, 0.5h and 0.25h, with h being the models height, respectively. In addition to the pressure readings an overall force measurement was taken during each test setup and overall drag coefficients were able to be calculated. Tests were performed at Reynolds numbers of 1.98×10^5, 3.95×10^5, 5.92×10^5 for each clearance.

The second phase of testing was similar to the first, but utilized an end plate that attached to the trailing edge of the model. This test used a end plate with tabs on two normal sides of the model. There were three tabs on each side, with a height of 0.03h.

This thesis verifies that the addition of tabs to the trailing edge of a bluff body is unsuccessful in reducing the overall pressure drag due to vortex shedding along the trailing edge, as presented in previous work. However, it can also be seen that the introduction of a stationary ground plane has an obvious effect on the base pressures of a bluff body and that the bounded flow characteristics of a bluff body in ground proximity lead to an overall lower base pressure. Additionally, it was observed that ground effect influence alters the vortex shedding seen over a bluff body in an unbounded flow, and creates an asymmetry in shedding.

ACKNOWLEDGMENTS

I would like to thank many people for their support, help, and dedication during this process. First I would like to thank Dr. Tso for agreeing to agree to take me as a graduate student and for his guidance and knowledge as I navigated through the thesis. Additionally, I would like to thank Cody Thompson. His help and knowledge in manufacturing components and maintaining the wind tunnel in an operating condition was invaluable during this process. A big thanks to my family, for their support and encouragement during this process, and providing me with so many opportunities. To Rachelle, thanks for being a great lab assistant, and an even better date. Lastly, thanks to Aleksey and Christian, who helped me technically with my project, and outside of the classroom as well. I don't know which one of your couches I preferred more during my SLO trips.

TABLE OF CONTENTS

LIST OF TABLES

LIST OF FIGURES

NOMENCLATURE

δ	Boundary layer thickness
ε_S	Solid blockage factor
ρ	Density
ν	Kinematic viscosity
A_F	Test model frontal area
A_T	Test section cross sectional area
C_d	Coefficient of drag, $\frac{D}{q_\infty S}$
C_p	Coefficient of pressure, $\frac{p-p_\infty}{q_\infty}$
$C_{p,b}$	Base pressure coefficient, $\frac{p_b-p_\infty}{q_\infty}$
H	Ground clearance
L	Length of model
Re	Reynolds number, $\frac{U_\infty L}{\nu}$
U_∞	Free stream velocity
WIG	Wing in ground effect
h	Height of model

l_y	Height of tabs
l_z	Width of tabs
p_∞	Free stream pressure
p_{tot}	Total pressure
q_∞	Free stream dynamic pressure
u,y,w	Streamwise, spanwise, and normal velocity
x,y,z	Streamwise, spanwise and normal coordinates

1. INTRODUCTION

This thesis investigates the passive drag reduction for a square-base bluff body with a stationary ground plane. For all previous work[5,6,7] leading up to this thesis, data was collected and analyzed for a bluff body in unbounded flow, and each attempted to find ways to decrease overall pressure drag through passive and active measures.

For bluff bodies, the largest source of drag comes from pressure drag, with the majority caused by the large, blunt trailing base region. Due to the ninety degree turn at the trailing edge of the body, the airflow is quickly separated from the vehicle, resulting in Von Karman vortices. These vortices create a low pressure region along the bluff base, drastically increasing overall drag. By controlling these vortices, mainly through attenuation and forcing, it is theoretically possibly to decrease the strengths of the vortices and the overall drag experienced by the body.

In typical aircraft aerodynamics the flow is considered unbounded and the streamlines have unlimited room to form around the body. However, in bounded aerodynamics the flow around the object is limited, or bounded, by a surface such as walls, water, or the ground. Ground effect aerodynamics is the study of the flow properties when a vehicle such as a car or an aircraft is operating in proximity to the ground. For aircraft, this effect can most often be experienced during both take-off and landing. By harnessing this effect aircraft can increase lift while decreasing drag[1], improving the efficiency of flight. For decades, research has been conducted on building viable Wing In Ground Effect Vehicles (WIGs)[3] . However, WIGS are still designed with streamlined, aerodynamically minded bodies, and the ground effects can be tailored to suit each vehicle's operation.

For large tractor trailers, heavy trucks, and even buses, the shape of the vehicle is dictated by the cargo it carries, vehicle regulations, and manufacturing costs. This leads to body shapes that resemble large, square bluff bodies that often have poor aerodynamic performance. Recently there has been a lot of research looking into decreasing the drag force on such vehicles through aerodynamic tractor design and add on devices, driven by the desire to increase efficiency in the wake of rising gas prices[12].

This thesis will experimentally investigate the overall effect of drag on a bluff body as proximity to a stationary ground plane increases. Additionally, passive, tabular drag reduction devices attached to the vehicles trailing edge will be investigated as a means of reducing base pressure drag.

2. BACKGROUND

In typical aircraft aerodynamics the airflow over a wing can be considered unbounded, meaning that the streamlines have unlimited room to expand on both the upper and lower surfaces. On the contrary, in a bounded case, in which a boundary exists close to the wing, there is an important interaction with the flow field around the wing. For airfoils, a boundary near the bottom surface can increase overall efficiency by increasing lift and decreasing drag. This phenomenon can often be experienced during a typical aircraft's takeoff and landing; as the aircrafts wing is closer to the ground, a larger lift force is generated[1]. This is commonly referred to as "ground effect" and has been researched for decades as an alternative to normal flight in an effort to raise efficiency, and ultimately lower fuel costs. Below in Figure 1, the effect of a nearby boundary on a wings pressure distribution can be seen.

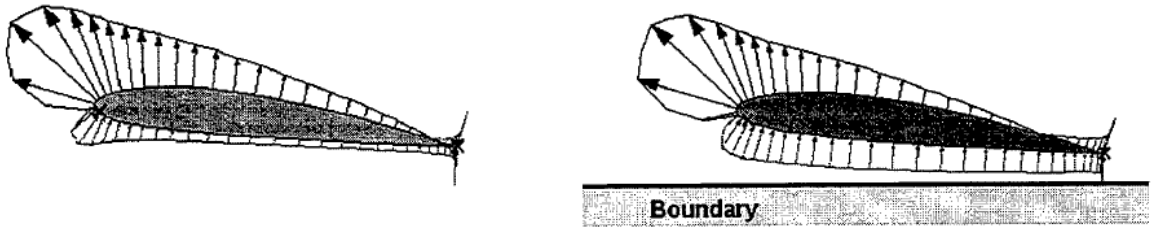

Figure 1: Surface Pressure Distribution With and Without Ground Effect[2]

Wing in Ground Effect (WIG) vehicles have been a subject of study for decades, with applications for vehicles ranging from military operations to large transport aircraft. Starting in the late 1970's Russia began development, test, and operation of a class of "ekranoplane" designed to fly low and fast over the ocean surface, whilst being able to carry, and fire, missiles. Most recently, Boeing[2] investigated the possibility of a large

cargo ground effect vehicle nicknamed "Pelican" which would utilize the increase in efficiency a wing experiences while flying in ground effect. However the program has, to public knowledge, become defunct.

Ground effect does not only affect aircraft, but has applications to ground vehicles as well. Ground effect plays a key role in the aerodynamics of every road vehicle, whether it is a Formula car or large transport truck. The aerodynamic characteristics of a ground vehicle are difficult to model accurately in a wind tunnel however, with the most precise results requiring expensive equipment in order to obtain. The key issue of modeling ground interactions in a wind tunnel comes from the boundary layer formation in a wind tunnel which does not depict the real situation. As can be seen in Figure 2, the air moves in relation to the test object in a wind tunnel, forming a boundary layer on both the model underbody and the ground surface itself. In a real world scenario, the vehicle moves in relation to the airflow, creating a boundary layer on the under body of the vehicle itself, but not on the road.

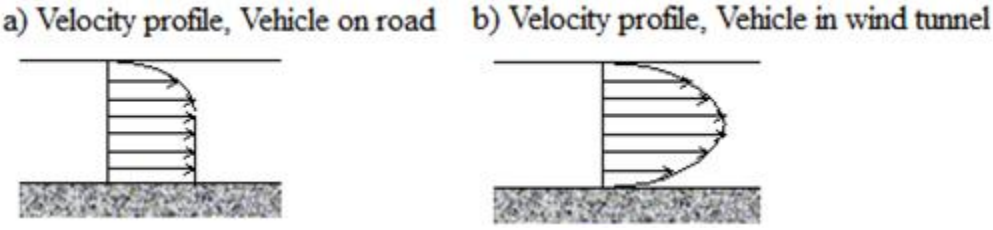

Figure 2: Boundary Layer Comparison[22]

There are many methods that can be used to effectively measure ground effect aerodynamics in a wind tunnel, the most popular of which are shown in Figure 3. This figure depicts four different methods for simulating ground effect: the image method, combination sucking and blowing, a lifted model with a stationary ground plane and a

moving belt technique. For each method there exists a tradeoff between complexity/cost and accuracy of results obtained, while different methods can be better based on the experiment at hand. A trade study, which will be described later on, is usually performed to find the most efficient method for the desired test at hand.

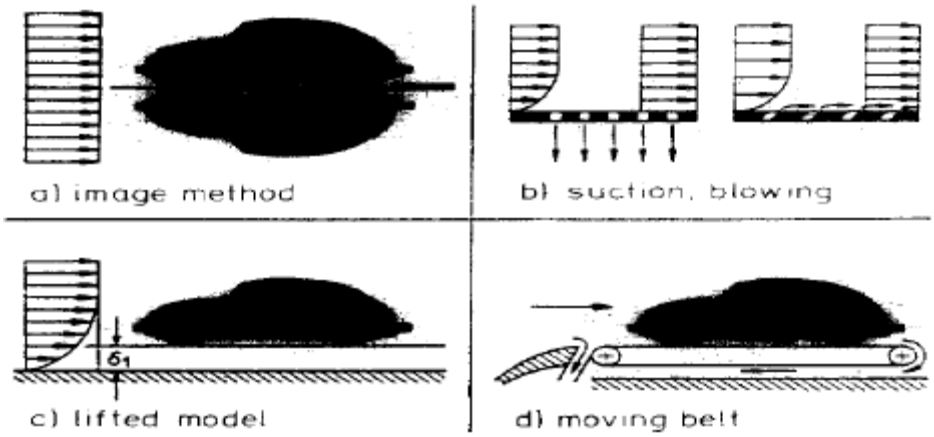

Figure 3: Testing Methods for Ground Effect in Wind Tunnels[9]

As mentioned earlier, the main consideration when deciding which method to use is the difference in boundary layer build-up in the wind tunnel. It is of utmost importance to understand the interactions between the body being tested and the level of accuracy required for results, and to choose the proper testing method that will most closely mimic real world results.

3. LITERATURE REVIEW

This thesis looks to further investigate the relationship between drag reduction devices and bluff body with a blunt trailing edge as previously studied by Park et al[4] with a 2D body and Pinn[5], Erlhoff[6], and Barker[7] at Cal Poly on 3D bluff bodies. While each of these studies focused on the drag reduction of a bluff body with a blunt trailing edge using both active and passive devices, all of them were conducted in a nearly unbounded flow, with the closest bounding surfaces being the test section walls. For this research, it was important to find and analyze previous experiments that were performed in a bounded case, yet still had similar model geometries.

Pinn[5], who used a rectangular based bluff body model with an aspect ratio of four, found that the addition of tabular devices on the trailer edge of a bluff body led to an overall decrease in drag at the lowest Reynolds number tested, by as much as 37%. However, at higher speeds, drag was actually increased with the addition of tabs. Pinn concluded that the tabs were effective in attenuating the Karman vortex shedding, which created a higher, more constant pressure distribution over the entire base region of the body. However, follow up research performed by Innes and Carlson[18], as well as independently in the early stages of this research, were unable to duplicate Pinn's results.

Erlhoff[6] investigated the effect of distributed forcing on the overall drag reduction of a bluff body similar to Pinn's with an elliptical leading edge and found that with a combination of sucking and blowing, base pressure on a bluff body could be increased, thereby decreasing drag. However, the electrical energy required outweighed the drag savings at the higher, more applicable speeds, and Erlhoff concluded that current

technology does not provide efficient means to actively reduce bluff body drag via forcing.

This study was followed by Barker[7] who investigated the effect of trailing edge tab height on attenuating vortices. Barker used a 1:1 aspect ratio model with three different base plates, each with a different tab height along two sides. By measuring boundary layer height at the trailing edge of the model, Barker was able to find a theoretical optimal tab height that could be used to attenuate vortex shedding and effectively raise mean base pressure. Results showed that for each tab height, and for each Reynolds number tested, overall drag on the body increased over the non-tabbed baseline case. Pressure measurements on the body base showed a decrease in base pressure by as much as 0.045 at the low Reynolds number, while drag force measured from a sting balance showed an increase in overall drag for all tab cases. Additionally, hotwire anemometry indicated a large spike in the energy spectrum for both the non-tabbed, as well as each tabbed case, indicating the failure of the tabs to attenuate the vortices. In conclusion, Barker stated that his findings were not in agreement with Pinn at low Re, and that tabular devices on the trailing edge of a 3D bluff body were not effective in reducing overall drag at any tested Reynolds number.

As mentioned, each of these previous studies performed at Cal Poly were performed under approximately unbounded aerodynamic conditions. In road vehicle applications, the ground plays a critical role in the aerodynamic performance of a vehicle, so special consideration must be taken to effectively model the bounded case. Research has been extensively performed on the proper techniques for mimicking the correct aerodynamic properties caused by the road introduction. Kim and Geropp[8] investigated

the effects that various ground clearances have on 2D bodies, with both moving and stationary ground planes. The team found that while drag coefficient remained similar with both the moving and stationary ground planes, the lift coefficient varied significantly between the two cases. This discrepancy in lift between ground clearances is only seen for small ground clearances typically below .2h, as proven by Fago et al[9], Garry[10], and Kim and Geropp[8]. It was found that as the ground clearance increases, the difference in results between a moving ground plane and stationary ground plane decreases. Overall, it can be shown that for ground plane clearances ~0.2h (h, the model height) and above, stationary ground planes can give satisfactory results for bluff bodies.

In 2006, Kim et. al.[11]. performed a study on the effect that a moving ground plane has on the enhancement of aerodynamic characteristics on a bluff body. Passive control was achieved by the addition of fences horizontal and vertical to the lower trailing edge of the bluff body, near the ground plane, and aerodynamic characteristics were analyzed for stationary and moving ground plane cases. The test setup is shown in Figure 4 below.

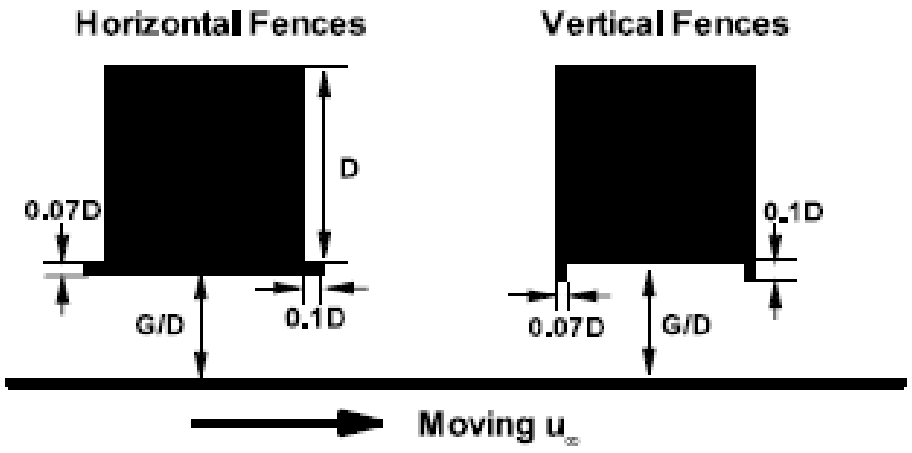

Figure 4: Kim et. al. Experimental Model

Horizontal fences were found to have lower drag at small gaps with a stationary ground plane than the bare model at the same gaps, but less so with a moving ground plane. However, vertical fences were found to increase drag above the bare model at the same gap range, which is attributed to the blockage of the gap flow at the smaller clearances.

Numerous studies have also been performed on potential drag savings via passive devices on a full scale bluff body. In 2012, the National Research Council Canada[12] released a technical report on aerodynamic drag reduction devices for heavy trucks and busses. They found that at higher speeds, up to 70% of fuel consumption could be attributed to aerodynamic drag. Full size tractor trailers were analyzed, and it was found that majority of aerodynamic drag was caused by the tractor trailer gap, the underbody, and the base drag of the trailer. However, in their research, they found that vortex generators intended to influence flow separation at the rear of the trailer were ineffective in reducing overall drag. In fact, according to a paper this study cites, Leuschen and Cooper[13] found that there was a measurable increase in drag, and in turn fuel consumption, of greater than 1% for the devices they used. In tests performed by Leuschen and Cooper, vortex generators were placed on each side of the trailer, just before the trailing edge. Six generators were placed on each side, each angled at 30 degrees. The study states that the base pressure of the trailer was unaffected due to the vortex generators, so the overall drag increase had to be due to the drag force caused on the vortex generators themselves.

In 2008, Gurlek et al[16] studied the flow structure around a three dimensional bluff body using PIV measurements and flow visualization. They found that the shear layer of emanating from the model top dominated the wake region, resulting in a jet like flow

emerging from the gap between the lower surface of the model and the ground plane, creating a tight, base corner vortex. In the horizontal direction, it was seen that that the stream wise velocity component had a flow reversal region forming from each of the sides of the model in the near wake, up to a distance equal to 1.07 times the models height.

As recently as 2010, Shi et al. studied wake characteristics behind a 2D square cylinder. In the experiment, Shi et al. used a false floor with a fully turbulent boundary layer, achieved with he placement of trip wire and sandpaper on the leading edge of the ground plane. The experiment concluded that for the larger ground clearance of .5h, vortices were alternatively shed from the top and bottom surfaces of the model. However, at the lower ground clearance of .25h, much weaker vortices were found, with a lower region recirculation zone that was deemed to be under the influence of vortices buried in the upper shear layer. Figure 5 below shows the time-averaged streamwise velocity profiles for both ground clearances tested by Shi et al, with H/h=0.5 on the top of the figure and H/h=0.25 on the bottom. It can be observed that at the lower gap width, the streamwise velocities are altered at the lower surface of the model, a sign of a low speed recirculation zone that bends upward and converges with the upper recirculation zone further downstream.

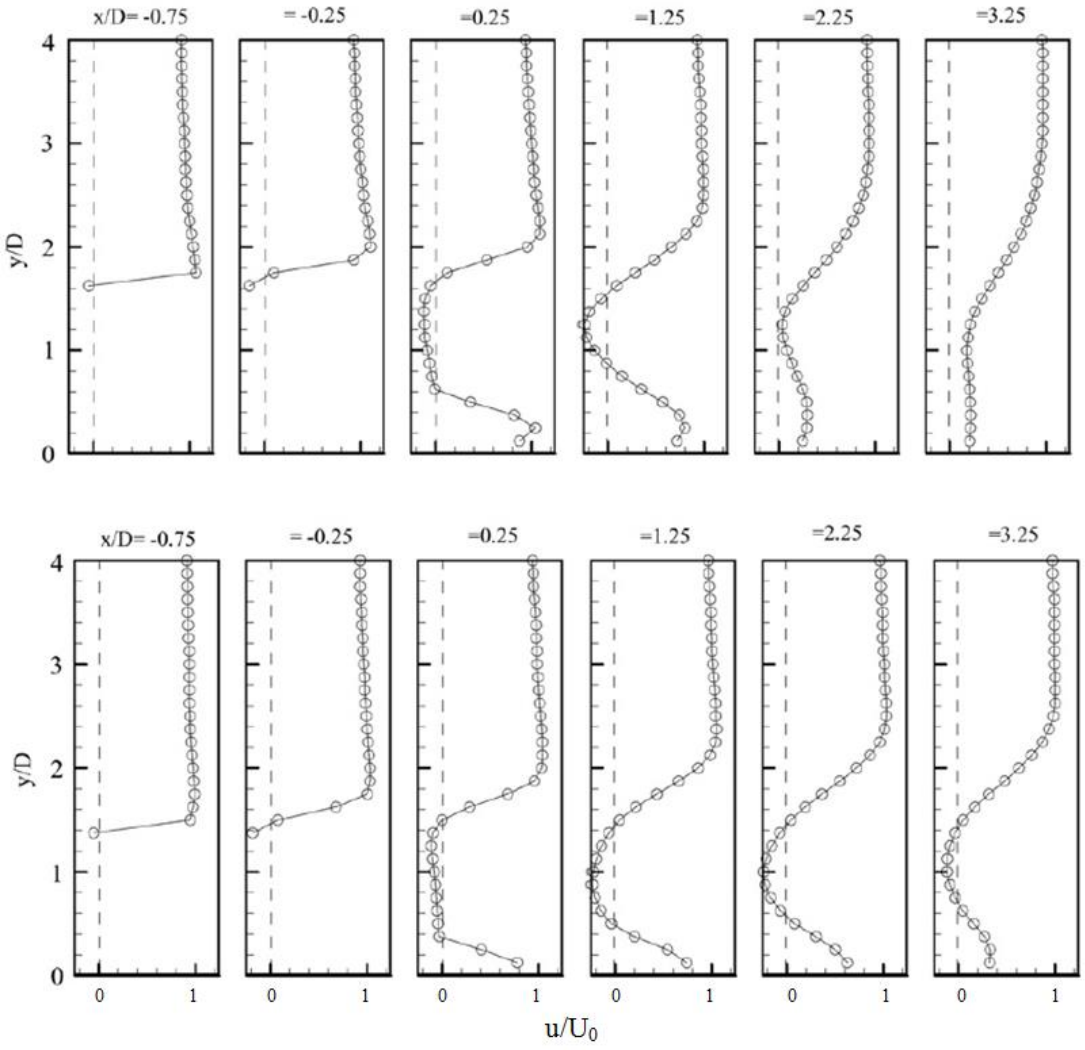

Figure 5: Time-Averaged Velocity Profiles from Shi et al.

Cai et al.[20] investigated the effect of wavy trailing edges on vortical shedding at the base of a bluff body via direct numerical simulations. Testing at a Reynolds number of 2500 with respect to model height, Cai et al. performed numerical analysis on wavy edges ranging from L=3h to L=7h, and compared those results to 2D and 3D bluff based results. It was concluded that moving average form drag for the sinusoidal wavy trailing

edges were within the predicted upper and lower bounds of the 3D case, with the L=5h test model providing the largest decrease in base drag.

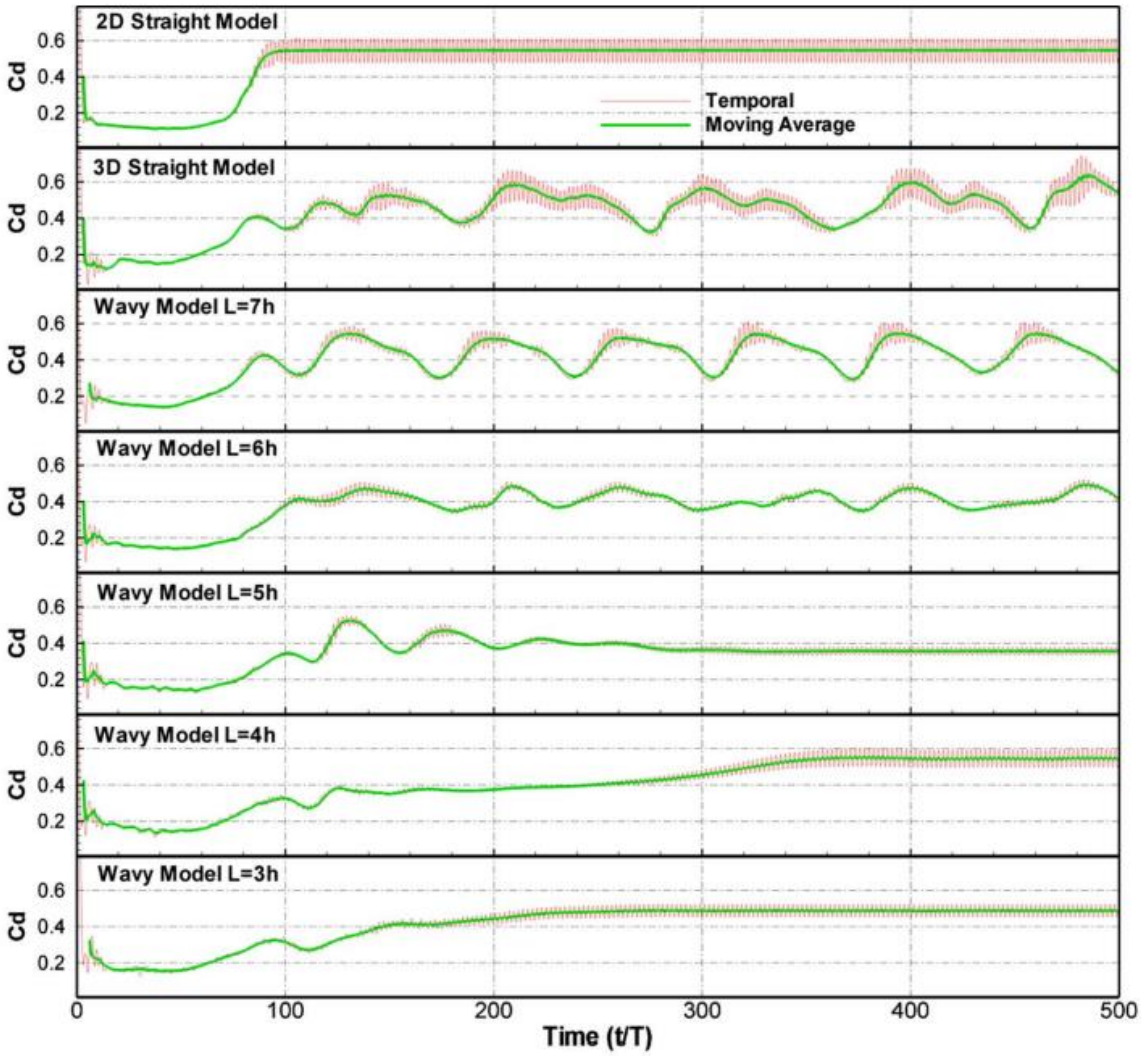

Figure 6: History of the drag coefficient for the various models investigated[20]

Straatman and Martinuzzi[21] performed an investigation the boundary layer thickness had on vortex shedding from a square cylinder near a wall, via computational models. They discovered that there existed a critical gap height at which complete suppression of vortex shedding occurred. However, for higher gap clearances, a coupled

shear layer motion was observed, that shifted to the far wake region as the ground clearance decreased. It was found that the critical gap height, at which all non stationary activity was suppressed, was found to be between 0.25 and 0.28 times the model height, and was accompanied by a decrease in drag coefficient. Figure 7 below shows plots of that boundary layer thickness and gap height had on the calculation of drag coefficient in Straatman's analysis.

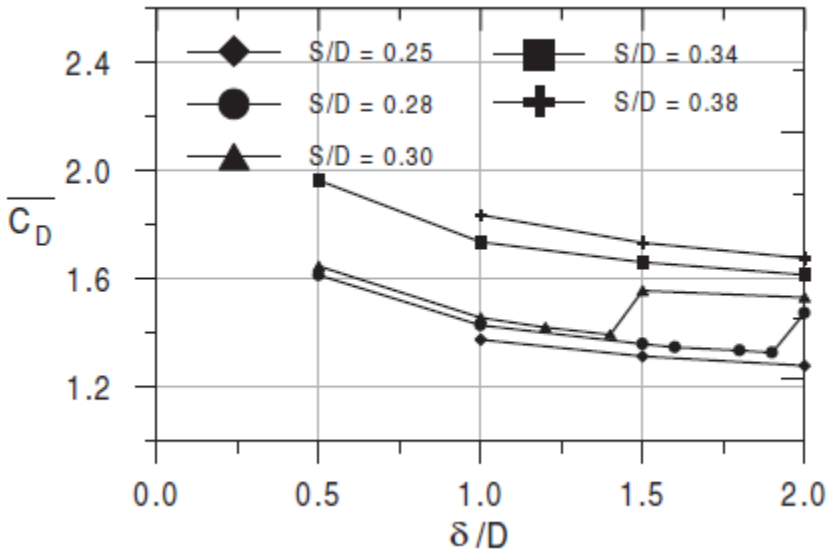

Figure 7: Influence of Boundary Layer and Gap Height on Cd

Due to the initial success of studies by Park et al. and Pinn in reducing drag on a bluff body in unbounded flow, the current research is intended to focus on the drag reduction savings once a ground plane is introduced, and whether the unbounded and bounded flow properties were similar for a bluff body modeling a large trailer. However, the literature review showed that vortex generators were ineffective in reducing base pressure drag of a bluff body. In fact, most research, as well as Barker's Cal Poly thesis research suggests that drag is increased as a result of adding vortex generators. This paper attempts to investigate and clarify the relationship between bluff body pressure

drag and vortex shedding, and further studies the aerodynamic effects of introducing a ground plane to mimic real world bounded aerodynamics.

4. EXPERIMENTAL APPARATUS

4.1 Experimental Model

The bluff body model used in this experiment was designed and used in previous experiments, and its schematic can be seen in Figure 8. The body is constructed of 6061 aluminum and has cross sectional base dimension of 12.7 x 12.7 cm (5 in. X 5 in). It has a circular nose with a radius of 6.35 cm (2.5 in) and a total overall length of 29.845 cm (11.75 in).

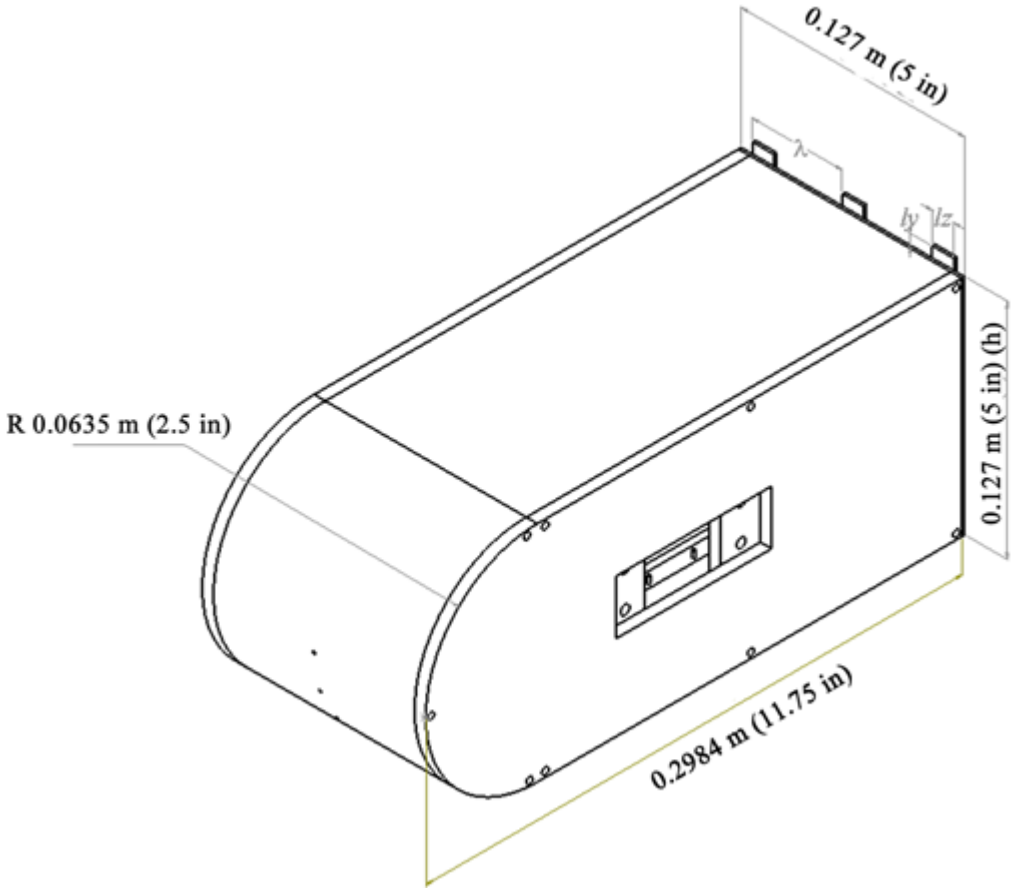

Figure 8: Bluff Body Model Dimensions

On the bluff trailing edge are 44 pressure ports: a row of 16 in the normal direction, perpendicular to the ground plane, equidistant from the edges of the base, and 2

rows in the spanwise direction, parallel to the ground plane, each with 15 pressure ports. In the normal direction, one row is equidistant from each edge of the base, placing it in line with the center tab, while the other row is equally spaced between the top and middle tabs. A schematic of the pressure ports can be seen in Figure 9.

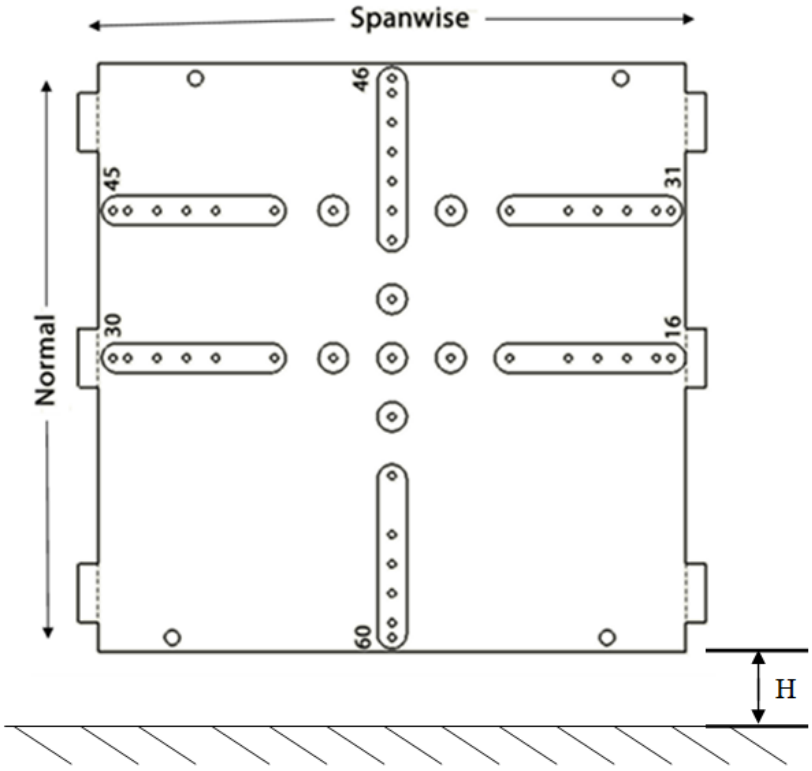

Figure 9: Pressure Port Layout

Each pressure port is made of 1.5875mm (1/16th inch) stainless steel tubing, which connect to Tygon PVC tubing internally to the model. These tubes run through the model support strut and out of the wind tunnel, at which point they connect to the Scanivalve for data collection. The ports are spaced 3.175mm (1/8th of an inch) near the edges, with the spacing increasing to 12.7mm (1/2 inch) in the middle of the plate. This provides more accurate pressure readings near the edges of the base.

The model design incorporated removable base plates which allowed for many tab configurations to be tested without having to change the entire model. Each end plate screws into the base of the model, with slots cut out that allow for the pressure ports. This enables removal and switching of end plates without having to adjust tubing internally to the model, resulting in fewer inaccuracies in data due to changes in model orientation between tests. The testing performed in this thesis used two different end plates. The first end plate, seen in Figure 10, has three tabs on each normal side of the plate. Tab heights are 0.58 cm (0.23) inches, with a width of 1.27 cm (0.5 inches).

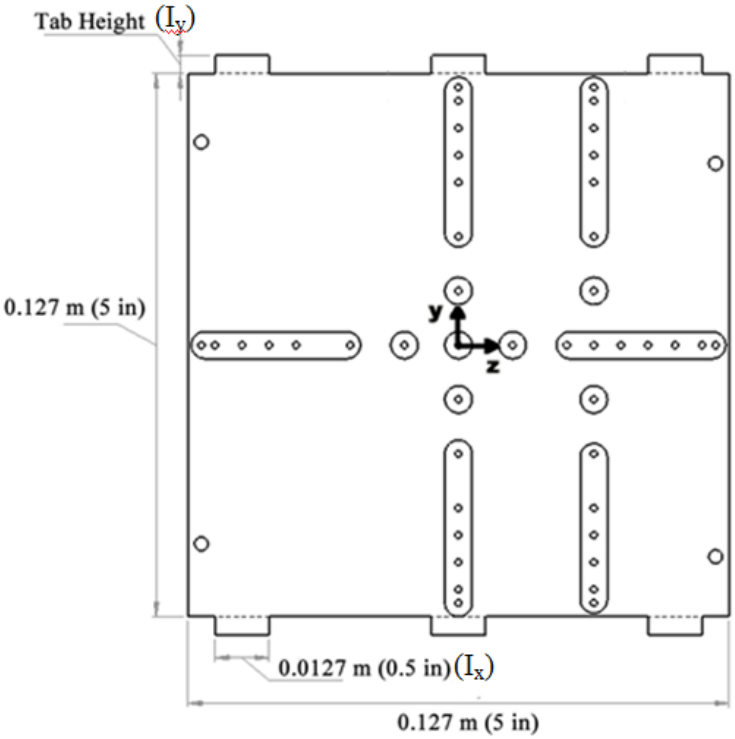

Figure 10: Base Plate Tab Dimensions

The model mounted to a steel strut that which could be connected to the sting balance in the wind tunnel. The strut was formed into a smooth airfoil shape to reduce any flow effects it would have on the test results, and is hollow on the inside to

accommodate 30 aluminum tubes within the interior of the strut and up into the model, where they can connect to the pressure ports. At the bottom of the strut, where it connected to the sting balance, the aluminum pressure tubing is connected to Tygon PVC tubing, which was run out of the tunnel and connected to the Scanivalve.

4.2 Experimental Ground Plane

There are many different ways of mimicking real world condition of road vehicle aerodynamics in a wind tunnel, with different options being preferred for different test setup and level of accuracy desired. When choosing a method for this experiment, three options were considered: a stationary ground plane, a moving ground plane, and a hybrid stationary ground plane. In a moving ground plane, the test model is placed above a belt that has the ability to move in the flow direction. This moving plane is then calibrated to move at the same speed as the wind tunnel flow, effectively accelerating the flow along the plane to the free stream velocity, eliminating the boundary layer. This method is preferred for the most accurate results, but is expensive, mechanically complex, requires ample space for installation, and has some very difficult technical problems to overcome. One such technical problem is that during operation, the moving ground plane may have the tendency to be sucked up and towards the model due to the low pressure region, causing a non-flat ground plane. There are methods to counteract this phenomena, but they are expensive and would have been difficult to implement in the existing Cal Poly wind tunnel. In contrast, a stationary ground plane utilizes a flat piece of material that is supported up and away from the wind tunnel floor. The model being tested is then placed on top of the ground plane for testing. In this situation, the large boundary layer that has been built up for the entire length of the tunnel passes underneath the ground plane and

the model, while a much smaller boundary layer develops on the ground plane under the model. In this way, the model can be tested with a very thin ground plane boundary layer, more closely mimicking the real world case of no boundary layer. This is a much simpler method for simulating ground effects, and is appropriate for larger ground height clearances. However, for ground clearances ~.15h and lower, a moving ground plane is preferred, as even the small boundary layer on a stationary ground plane can play a large role in the flow characteristics on the models underbody. Lastly, a hybrid stationary ground plane system was considered for this research. In this scenario, a stationary ground plane would be used, except the boundary layer built up on the plane would be suctioned out just prior to the model, eliminating the boundary layer altogether under the test model. This would have required that a complicated system be installed into the wind tunnel and would have created a blockage problem in our relatively small test section. After all the options were weighed, it was decided to use a stationary ground plane for this experiment. The main reason was that for typical bluff body road vehicles, the ground clearance is usually > 0.2h, so the accuracy of a moving ground plane was not required for the large gaps that would be tested. Additionally, both the moving and hybrid ground planes would have required extensive modifications to the wind tunnel, requiring both money and expertise outside the scope of this research.

The stationary ground plane was constructed of 1/8in thick 3003 alloy improved strength aluminum, and measures 0.91 m (3 ft.) wide and 1.07 m (3.5 ft.) in length. All edges of the ground plane were rounded to 0.15875 cm (0.0625 in) radius for flow considerations, with special attention paid to the leading edge round. At the back of the ground plane is a 0.15 m (6 in) flap that can be secured at various angular positions. This

flap was also constructed of 0.318 cm (0.125 inch) thick 3003 alloy improved strength aluminum and was attached to the ground plane with a 0.635 cm (0.25 inch) thick leaf piano hinge. By varying the position of this flap, the stagnation point of the flow was manipulated to ensure that it was on the leading edge, or slightly under, the ground plane, and, as is shown in later testing, allowed for verification of a laminar boundary layer for the entire length of the ground plane. On the top side of the ground plane are four female threaded sockets, mounted to the plane via a counter-sunk fastener on the bottom side of the ground plate. These sockets were used to fasten the threaded steel rods that supported the hanging of the ground plane from the tunnel ceiling.

The width of the ground plane was easy to decide, as we wanted it to extend as far from the model edges as possible, but was restricted by the wind tunnel walls. By making the width 0.91m (3 ft.), 0.15m (0.5 ft.) were left on each side of the ground plane to the tunnel wall, allowing for installation and removal of the ground plane without damage to either component.

Along the length of the ground plane ran two stiffening spars. These spars were added after initial tests showed questionable ground plane vibrations during the higher speed testing. Each spar is constructed from an aluminum U-beam, and is mounted to the ground plane via counter sunk fasteners on the bottom side of the ground plane. The leading edge of each spar was chamfered for aerodynamic considerations. The spar and rounded leading edge can be seen in Figure 11.

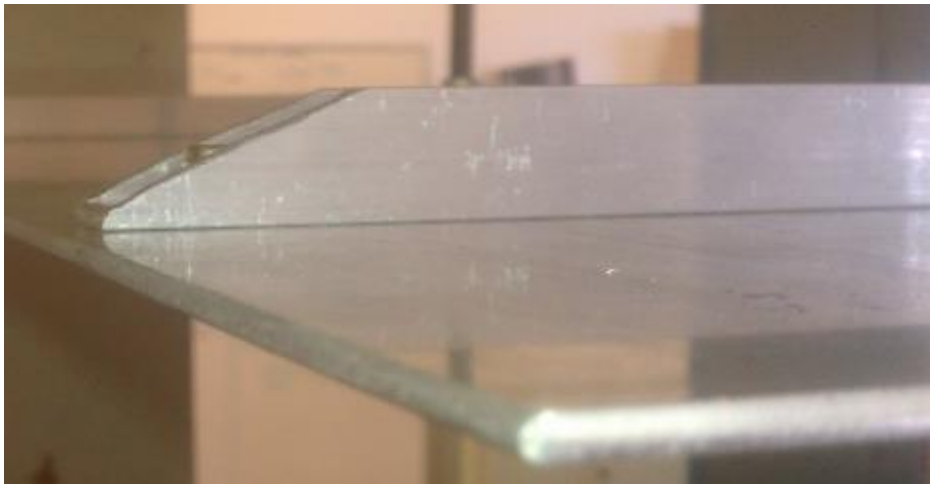

Figure 11: Support Spar and Ground Plane Leading Edge

Installed into the surface of the ground plane are 7 pressure ports, flush to the bottom surface of the plane. These ports are used to analyze the pressure gradient along both the length and width of the ground plane. In the lengthwise direction, the first pressure port is installed 5 inches from the leading edge. The next three are each installed another 6 inches from the previous. The 5th port is located 23 inches from the leading edge. Figure 12 below shows a drawing of the ground plane, with the port distances dimensioned. By reading these pressures the proper flap position was able to be determined. Initially tested flap configurations were chosen based on the literature reviews, and started with the flap in a 5 degree up (away from the model) position. The flap was then lowered in decrements of 2.5 degrees, until it was 5 degrees downward (towards the model) as the final test position. At each flap angle, the pressures along the plate were recorded, and the change in pressure at each port in each direction was analyzed. The goal was to find the flap position that would minimize the difference in pressure change at each port, resulting in a close to zero pressure gradient, indicating a laminar boundary layer.

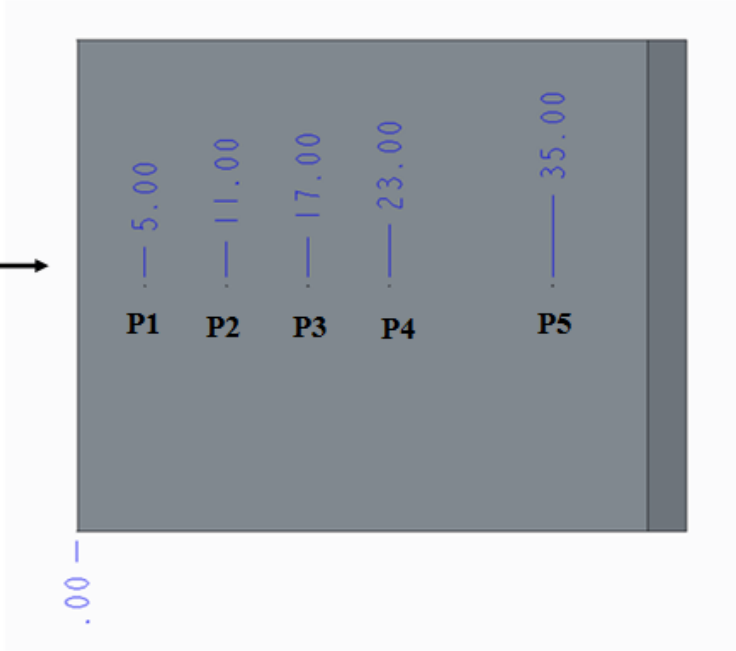

Figure 12: Ground Plane Pressure Port Locations

The ground plane is lowered into the wind tunnel via the existing window at the top of the wind tunnel test section. A new top window, which supported the installation of the ground plane, was constructed using rigid polyethylene. The dimensions of the top plane were kept consistent with the existing cutout in the test section of the wind tunnel, allowing for easy changing between windows when other tests needed to be ran. A total of four 4.45 cm (1.75") holes were cut into the top window to allow for four 1/2-10 ACME threaded rods to be inserted through, which would then screw into the ground plane socket fasteners. On the top of the top window each threaded rod had a 1/2-10 steel hex nut, used to control the height of the ground plane. In essence, this enabled the ground plane to hang from the top of the wind tunnel, above the test model, and could be adjusted to any height by adjusting the hex nuts along the threaded rod. Once the desired height was achieved for a particular test, a hex nut on the inside of the tunnel, one on each rod, was tightened up against the top window, locking the ground plane in place and

making it structurally resistant to unnecessary vibrations. Ground plane installation can be seen in Figure 13 below.

Figure 13: Ground Plane Installation

Figure 14 is a schematic of the ground plane and model installed together in the wind tunnel, indicating the ground clearance measurement in relation to the overall height of the model.

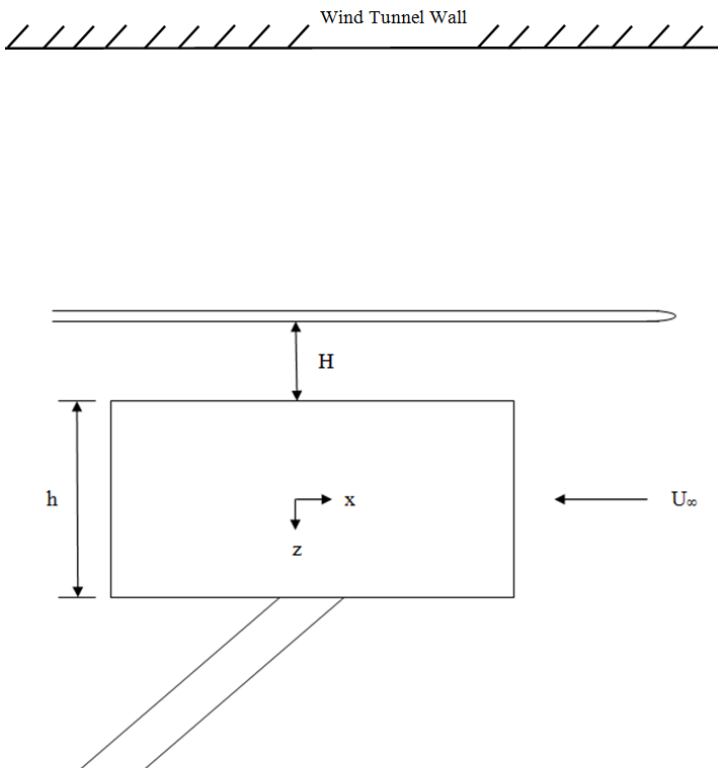

Figure 14: Installation Schematic

4.3 Wind Tunnel

All testing was performed in Cal Poly Aerospace Engineering's 0.9 x 1.2 m (3ft x 4ft) subsonic wind tunnel. The tunnel has a 3.7m by 2.7m (12ft by 9 ft) inlet that converges into the smaller test section. The Eiffel style (in draft open loop) tunnel is powered by a 125 horsepower, three phase electric motor that is controlled by an Allen Bradley variable frequency drive. A nine blade, fixed pitch fan is driven by the motor to suck air downstream and then expel it out of the building.

The test section contains an Aerolab sting balance that utilizes a load cell to measure forces in the axial, normal, and roll directions. This sting balance is able to be controlled by a LabVIEW VI, which enables pitch changes in 0.1 degree increments and allows for instantaneous data collection during testing. Additionally, the sting balance has

variable yaw control via a screw thread wheel turning system mounted under the wind tunnel. Total travel in the yaw direction is +/- 2.0 degrees. Figure 15 shows the exterior of the wind tunnel, with the inlet visible at the far end.

Figure 15: Cal Poly 3' x 4' 70 MPH Subsonic Wind Tunnel

4.4 Scanivalve Pressure Sensing

Pressures readings were collected by a ZOC33/64P-X1 Scanivalve pressure scanner. Pressure tubing was connected to the pressure ports internal to the test model, and then ran down the steel strut and out the tunnel, where they connected to the Scanivalve. The scanner has 64 ports that can be read in succession, with the variation of timing between port readings being chosen by the tester. The Scanivalve connects to 65psi compressed air used for calibration functions. The first 32 ports were used for all tests performed. These ports have an input range of +/- 10 inches of water, and an accuracy of +/- 0.15% of full scale reading.

The Scanivalve converted each port pressure into a voltage, which was then sent to and amplified by a RAD3200 analog to digital converter. The wind tunnel lab computer was connected to the converter, so all data was able to be acquired real time for analysis. All data from the Scanivalve was output into a .dat file, which were loaded into MATLAB for post processing and analysis.

Before testing with the Scanivalve, it was imperative that the unit had proper time to reach full operating temperature. Once a stable temperature was reached, as monitored by the RAD program on the lab computer, the Scanivalve could be zero calibrated and testing could begin.

4.5 Sting Balance

The wind tunnel test section contains an Aerolab sting balance that can be used to mount models and measure forces and moments in 6 DOF. The sting balance can be raised to three discrete heights in the test section; however for all testing performed in this thesis the balance remained in the lowest position. Additionally, the sting balance has independent angle of attack and yaw control. Angle of attack control is achieved through a LabVIEW VI on the lab computer, which is connected to control the sting balance. The sting balance converts its angular position to a voltage, which can then be read, and adjusted, by the LabVIEW program to achieve the desired angle of attack, with the ability to change the angle in increments of 0.1 degrees. Yaw directional control was achieved with a manual fly wheel, which rotated a screw thread that would rotate the entire sting balance, with the least scale reading on yaw position of 0.1 degrees.

Built into the sting balance are strain gages used to measure a force in each of the six degrees of freedom. Each of these strain gages had the ability to send a voltage

through a student-made amplifier and then to a data acquisition card (DAQ), which was connected to the lab computer. The same LabVIEW VI that controlled angle of attack was also used to collect the voltages from each of these strain gages. The LabVIEW program allowed for the choice of number of samples and frequency of voltage readings taken from each strain gage, enabling full control of data sampling depending on the test.

Prior to collecting sting balance data, a calibration had to be performed. In order to calibrate the sting balance, a weighted pulley system was used. Weights ranging from 1lb to 5 lbs., in one pound increments, were hung from the end of the sting balance, and over a pulley, for both the axial and normal directions, visually shown in Figure 16. Voltages were recorded for each weight, resulting in data points that correlated lbs force to voltage. When this data was fit with a line, an equation representing total force on the sting balance as a function of voltage reading was created. This equation was later used to find the forces on the test model during each experiment.

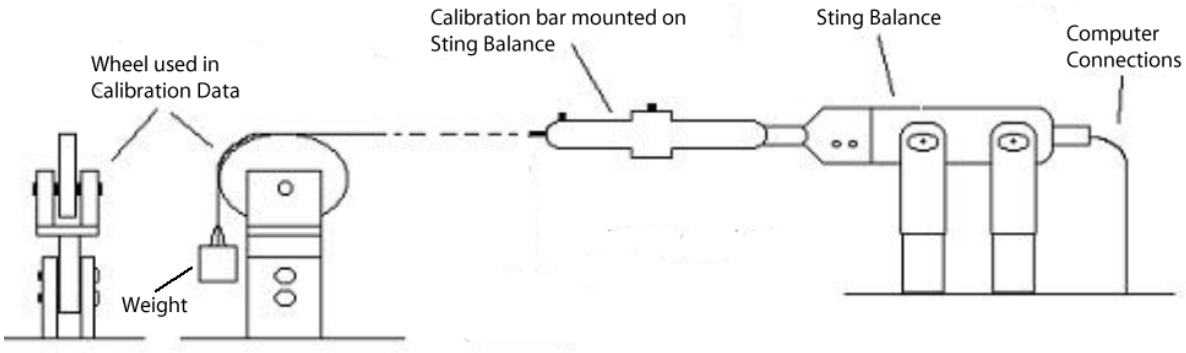

Figure 16: Sting Balance Calibration Set-Up

Figure 17 shows the results of the calibration and the relationship between axial force on the sting balance and the strain gage output voltage. The relationship is linear in nature,

with a coefficient of determination of 0.999, proving that the calibration was done properly and the sting balance readings were functioning properly.

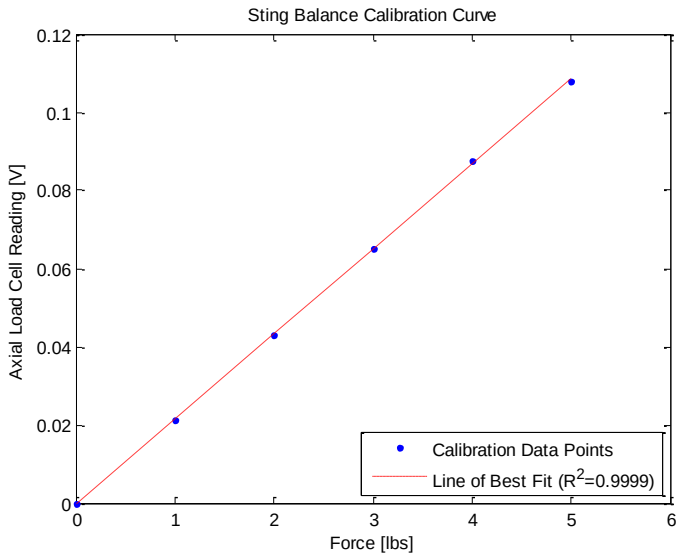

Figure 17: Sting Balance Calibration Curve

4.6 Pitot-Static Probe

A 1/8th inch Pitot-static probe was used to measure total and static pressures in the wind tunnel test section. Typically the wind tunnel utilizes a 0.635 cm (0.25 inch) Pitot-static probe that extends from the bottom of the test section, directly upstream of the sting balance. Since all testing was performed with the sting balance in the lower position, it was deemed that this position for the probe would interfere with the flow downstream around the model, so an alternate solution was found. A 1/8th inch Pitot-static tube was mounted to the wind tunnel wall and extruded through a viewing window, as can be seen in Figure 18. The 1/4 inch pitot tube can be seen in the background of the figure.

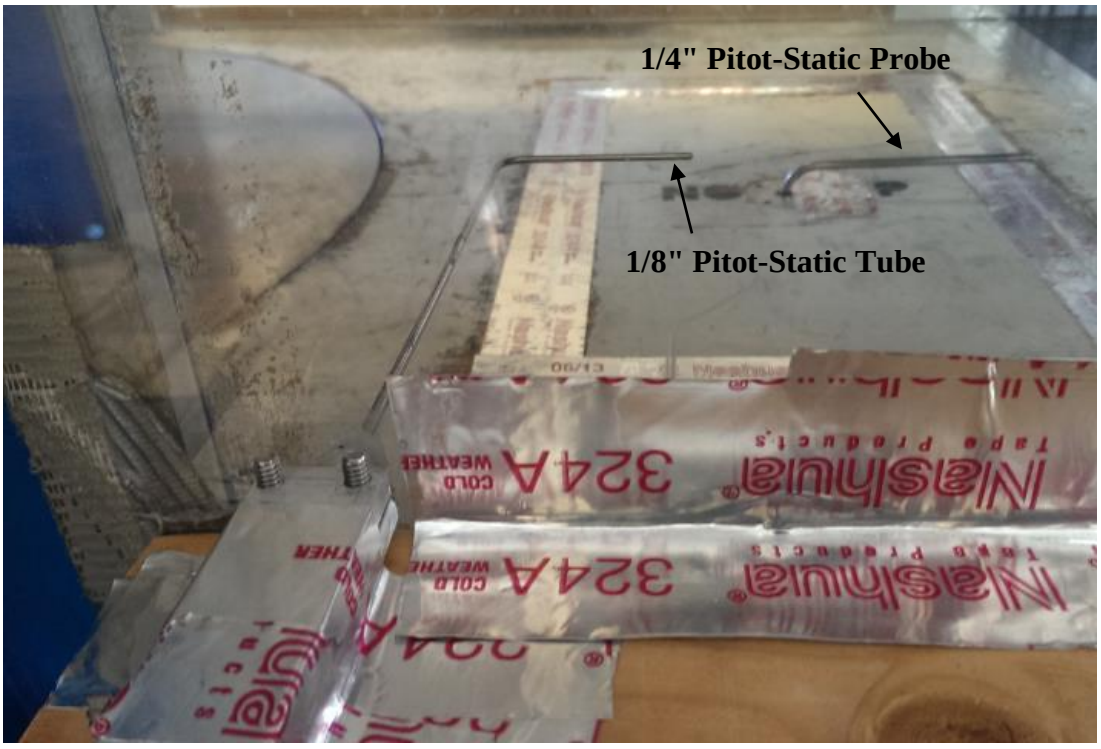

Figure 18: Pitot-Static Tube Installation

This pitot probe was situated so that the stagnation pressure measurement occurred vertically in line with the leading edge of the ground plane. As will be discussed later, tests were performed to ensure that the introduction of the ground plane and model did not have a major effect on the pressure readings of the pitot-static probe.

5. PROCEDURE

5.1 Wind Tunnel Calibration

During the course of the experimental testing, the wind tunnel became non-operational for a period of 10 months due to a broken controller. Once a new controller was received and installed, calibration had to be performed in order to correlate wind tunnel fan RPMs, regulated by the controller, to actual speeds seen in the test section. The VFD was able to accept manual inputs of RPM, and the dynamic pressure was able to be measured using a pitot tube set up in the center of the test section. By varying the input RPM and calculating the resulting test sections speeds, a correlation between fan RPM and test section speed was found. This initial calibration resulted in having a rough estimate of tunnel speeds based on RPM, which was the controlling input, during test initialization, and allowed for smaller adjustments to RPM to hone in on exact tunnel velocities as measured during testing. The calibration graph can be seen in Figure 19 on the following page.

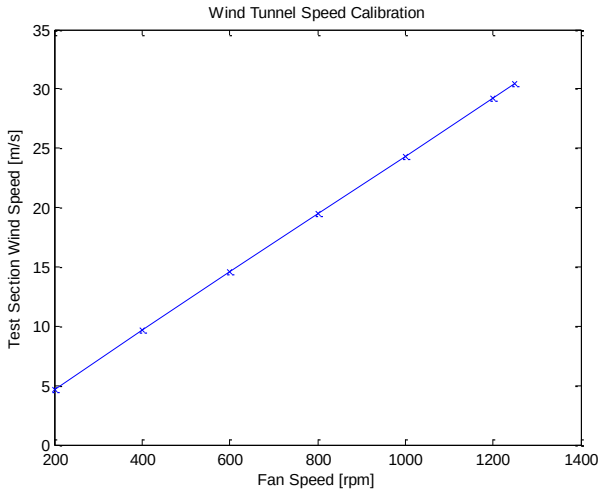

Figure 19: Wind Tunnel Calibration Curve

5.2 Ground Plane Boundary Layer

In order to verify the construction of the stationary ground plane it was important to measure and analyze the boundary layer along the length of the plate as well as the flow properties at the leading edge of the plate, to ensure that there was no local flow separation across the leading edge. A smaller, laminar boundary layer would be ideal for testing, however at the higher speeds it is impossible to keep a laminar flow across the length of the plate. Ideally, Reynolds numbers under 500,000 would correlate to a laminar flow over a flat plate, but, more realistically, laminar flow is present at Reynolds numbers of ~300,00 and below, mainly due to roughness in the plate surface. In Table 1 the Reynolds number for each test speed can be seen. Additionally, the Reynolds number was calculated at two locations: the first at the trailing edge of the model, and the second at the end of the flat plate, just prior to the flap.

Table 1: Theoretical Reynolds Number for Each Test Velocity

Tunnel Speed [m/s]	Reynolds Number [x=0.61 m]	Reynolds Number [x=1.02 m]
5	1.88×10^5	3.14×10^5
10	3.77×10^5	6.28×10^5
20	7.53×10^5	1.26×10^6
30	1.13×10^6	1.88×10^6

It can be seen that a laminar flow is only possible at the lowest flow speed of 5 meters per second for the ground plane in this experiment. While higher Reynolds number laminar flow might be possible under carefully controlled conditions, those conditions were not achievable in this experiment. Namely, the ground plane was not purposely set in a

favorable pressure gradient orientation. That is, the orientation of the ground plane, with respect to the incoming flow, was dictated by the orientation of the model in the test section, as it was imperative to achieve a symmetric pressure distribution around the model, requiring the ground plane to be parallel to the test model base. For every other test case, we would expect the boundary layer to be turbulent at the trailing edge of the ground plane. However, this can be expected when using a stationary ground plane for ground effect testing, and is satisfactory for larger ground clearances. Fago[8], in his research on the effect of ground simulation on flow around vehicles in a wind tunnel, simulated a stationary ground plane by using a fixed plate that was greater than 1.625m in length, with a precise dimension not being reported. However, the test he performed was ran at 20 m/s, which would create a turbulent boundary layer over the fixed plate he installed under the model. Additionally, Razenback et al also performed ground effect testing in a wind tunnel using a flat plate to simulate the ground. In this their experiment, the ground plane measured 1.83 meters in length with tunnel speeds being tested up to 40.2 m/s, or a Reynolds number correlating to 1.5 million based on the model chord length.

A stethoscope was used to qualitatively assess the characteristics of the boundary layer along the plate. By using a stethoscope attached to pressure port, which was provided by Dr. Westphal of the ME department, the flow could be listened to, and the much noisier turbulent boundary layers could be distinguished from the quieter laminar boundary layers. In order to record this information, and put a quantitative aspect to it, a microphone was built that could be used to record this data. An omni electret microphone was used, and was wired to a 0.318 cm (0.125 inch) audio jack that could be plugged into

any computer. The microphone was then inserted into a Tygon PVP tubing that was connected to the stethoscope, allowing the pressure differential caused by the boundary layers to be directly measured while minimizing outside noise interference. In Figure 20 the microphone installation can be seen.

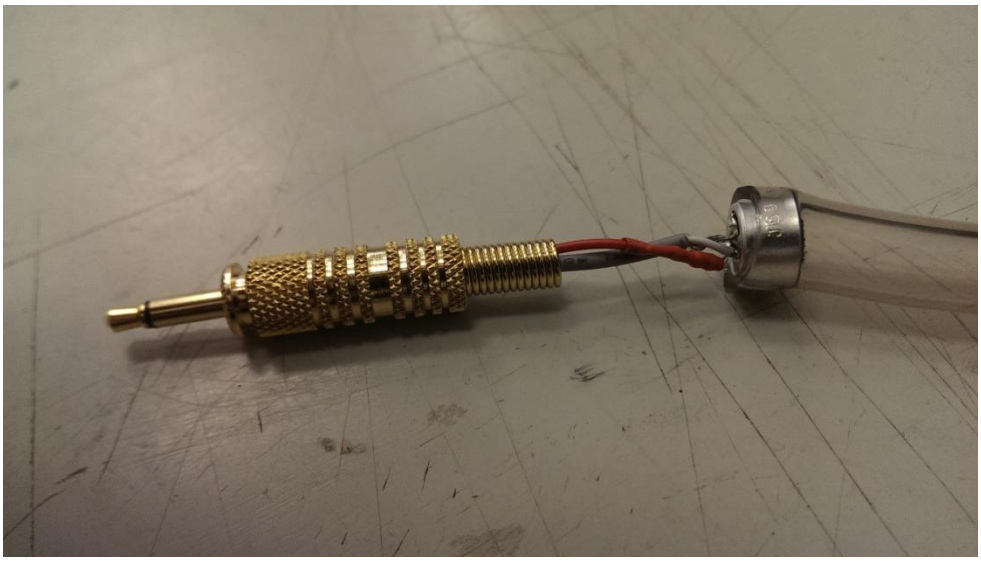

Figure 20: Microphone Wiring and Installation

In order to record and process the data, Audacity, an audio recording and processing program, was used. Audacity was able to not only record the sound caused directly by the boundary layer, but was also able to create waveform graphs, giving a visual representation of the boundary layer characteristics for the ground plane. With this method, the boundary layer built on the stationary ground plane was able to be observed at 5, 10, 20, and 30 meters per second.

Lastly, pressure from the pressure ports installed into the ground plane were used to determine proper flap configuration and verify laminar flow with a near-zero pressure gradient. By reading the pressure, the proper flap position was determined. Initial tested flap configurations were chosen based on the literature review, starting with the flap in a

5 degree up (away from the model) position. The flap was then lowered in decrements of 2.5 degrees, until it was 5 degrees downward (towards the model) as the final test position. At each flap angle, the pressures along the plate were recorded, and change in pressure at each port in each direction was analyzed. The goal was to find the flap position that would minimize the difference in pressure change at each port, resulting in a close to zero pressure gradient, indicating a laminar boundary layer.

5.3 Ground Plane Flow Separation

For flat plate aerodynamics it is important to ensure that the flow over the leading edge of the plate does not separate, causing unstable flow downstream and inaccurate measurement results during the test. To verify this, two different flow visualizations were used. The first was the tuft method, in which small pieces of yarn were attached to the surface of the ground plate over the entire length of the plate. When the tunnel was ran at 30 m/s, the yarns were watched for visual confirmation of attached flow. Along the entire length of the plate, it was seen that the flow stayed attached, as evidenced by the failure of the yarn to 'vibrate' against the plate. Figure 21, a screenshot taken from a video that was used for analysis, shows the fully attached tufts of yarn that indicate attached flow.

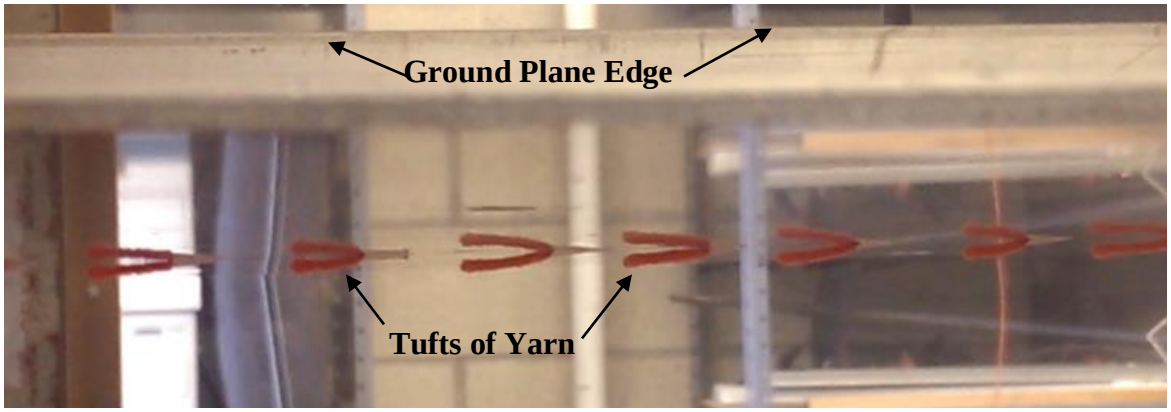

Figure 21: Flow Visualization Using Tufts of Yarn

The second source of flow visualization was smoke visualization. In this method, heated Rosco fog oil was inserted into the tunnel upstream of the ground plane. The smoke creates a streamline that follows the airflow down the tunnel, and flow around the ground plane could be observed. The smoke is moved spanwise across the length of the leading edge of the plate and watched closely for indications of flow separation. For the entire length of the leading edge, no flow separation was observed. Figure 22, a screenshot from the video taken for smoke visualization analysis, shows the experimental setup as well as a fully attached streamline down the center of the ground plate.

Figure 22: Smoke Visualization Over Ground Plate Leading Edge

5.4 Base Pressure Profile

Base pressures of the test model were measured for two base plate cases, at four ground clearances, and at three tunnel velocities. This resulted in 24 different test cases in which data was collected. At each case, both the normal and spanwise pressures were measured, with data being directly recorded to a .dat file which was post processed with MATLAB. The first configuration tested was the non-tabbed version with no ground plane in the tunnel, in which the tunnel walls acted as the nearest bounding surface to the

model. To start, the model's yaw and pitch were changed until a symmetric base pressure was found that showed signs of vortex shedding. From there, the ground plane was inserted into the tunnel and rotated through each of the three ground clearances: 1h, 0.5h and 0.25h. After all ground clearances of the non-tabbed case were tested, the tabbed endplate was installed onto the model, and each test was run again.

Table 2 below shows the test matrix detailing all test cases.

Table 2: Test Matrix

Model Configuration	Test Velocities	Ground Plane Clearance
Non-Tabbed	10 m/s 20m/s 30m/s	No Ground Plane .25h .5h 1h
Tabbed	10 m/s 20m/s 30m/s	No Ground Plane .25h .5h 1h

6. ANALYSIS

This section details the fundamental equations that govern bounded aerodynamics, and is meant to show the equations and analysis used to draw conclusions from the experiments performed.

6.1 Pressure Coefficient

The pressure coefficient, a dimensionless number, gives the pressure at individual points within a flow field compared to the free stream pressure. A pressure coefficient of 1 indicates a stagnation point, while a pressure coefficient of 0 indicates free stream pressure. In this experiment, the pressure coefficient was measured at the base of the model in order to determine pressure drag caused by vortex shedding. In addition, pressure coefficients were calculated at five discrete spots in the surface of the ground plane in order to measure and verify a zero pressure gradient along the ground plane. The pressure coefficient can be calculated by:

$$C_P = \frac{P-P_\infty}{q_\infty} = \frac{P-P_\infty}{P_T-P_\infty} \quad (1)$$

Where P is the measured pressure at each port on the model or ground plane, q_∞ and P_∞ are the free stream dynamic pressure and static pressure, respectively, and P_T is the free stream total pressure.

6.2 Drag Coefficient

The drag coefficient is the dimensionless drag force on a body and can be used to compare drag properties of different body geometries. When analyzing differences in drag properties for two similar bodies, or the same body across various speeds, it is often

beneficial to express the change in drag coefficient as a drag count, where a C_d of .0001 is a drag count of 1.

$$C_D = \frac{D}{q_\infty * S} \tag{2}$$

Eq. 2 gives the formula for calculating the drag coefficient, where D is the total drag force, q_∞ is the free stream dynamic pressure, and S is the cross sectional area of the model body. For testing in this experiment, total drag force is measured using the wind tunnel sting balance.

6.3 Reynolds Number

Reynolds number is a dimensionless ratio between the inertial and viscous forces of a flow and is commonly used to provide scaling of fluid dynamics problems. In wind tunnel tests Reynolds number is used to predict the similarity of flow properties and allows for the use of smaller scale models when testing. By matching the Reynolds number and model geometries two flows can be considered similar, allowing for testing on reduced models while correlating the data to actual, real world flows. A Reynolds number can also be used to characterize a flow regime within a fluid, as is used in this research to differentiate between laminar and turbulent flows. A transition Reynolds number is useful for predicting when a laminar boundary layer will become unstable and transition to a turbulent boundary layer and used in this paper to determine flow properties over the flat ground plate.

$$Re = \frac{u_\infty L}{v} \tag{3}$$

Eq. 3 gives the formula for Reynolds number, with u_∞ being the free stream velocity, L the characteristic length and v the kinematic viscosity. For the flat plate Reynolds number calculation, L will be the lengthwise distance away from the leading edge, while for the model the characteristic length is the model height, as to preserve the consistency of previous experiments.

6.4 Boundary Layer Thickness

The boundary layer thickness is the distance away from a body to a point where the flow velocity has reached free stream velocity, customarily defined as the point where the velocity is $0.99u_\infty$. This thickness is dependent on the type of boundary layer present over the model and is calculated differently for laminar or turbulent boundary layers. For laminar boundary layers, the Blasius solution gives:

$$\delta \approx \frac{5x}{\sqrt{Re_x}} \tag{4}$$

while the turbulent boundary layer thickness can be calculated by the empirical correlation:

$$\delta \approx \frac{.382x}{Re_x{}^{.2}} \tag{5}$$

In each equation, x is the distance at which the boundary layer is to be calculated and Re is the corresponding Reynolds number at that distance. It is important to have a understanding of the predictive thickness of the boundary layer, especially when testing ground effect. In this experiment, it was critical that a calculated boundary layer thickness be compared with a measured one, in order to verify that for the desired ground clearances to be tested the clearance was not smaller than the boundary layer thickness.

6.5 Blockage Factor

Wind tunnel blockage factor is the ratio of test article frontal area to total wind tunnel test section area, normal to the flow. In order to validate wind tunnel results, it is important to keep the blockage factor to a minimum, most often below 5%. If the blockage ratio is too high, the walls around the model can work to compress the streamlines, resulting in a local increase of fluid speed around the model and thus a higher perceived drag than that of a true free stream measurement. Equation 6 gives the blockage factor calculation:

$$\varepsilon_s = \frac{A_F}{A_T} \tag{6}$$

where A_F is the test setup cross sectional area and A_T is the test section cross sectional area, both normal to the flow. During these tests, the blockage factor is highest at the lowest ground clearance, due to the support rods having more of a frontal area. Even with this setup however, the blockage factor was found to be 5.1%, within a reasonable testing range. Maskell[14] derived an equation for a correction factor for separated flow measurements on bluff bodies, seen in Equation 7:

$$\frac{C_d}{C_{d,c}} = \frac{q_c}{q} = \frac{1-C_p}{1-C_{p,c}} = 1 + \eta C_d \varepsilon_s \tag{7}$$

where the subscript c refers to corrected values and η is the theoretical blockage coefficient, derived from the separated pressure coefficient of the model. However, this blockage factor was not applied to the results from this thesis. It was deemed that when testing with a stationary ground plane, the results are dependent on the blockage caused by the interaction of the model underbody and ground plane at low clearances, and apply a correction factor intended for free stream corrections would only hinder the actual

results. This decision is in line with the experiments discussed in the literature review section, which did not apply blockage correction factors for ground effect testing.

7. RESULTS

This section will show the results obtained from each of the aforementioned tests performed. It is meant as a presentation of individual test results, and to show trends across all the data collected. Engineering analysis, further data investigation and relationships, as well as possible explanations for the results obtained will be explored in the following discussion section.

7.1 Ground Plane Verification

Table 3 shows the pressure coefficients along the ground plane for various flaps angles. In the table, a negative flap position indicates the flap upwards, away from the model position, and vice versa. It can be seen that the initial test condition, with the flap 5 degrees up, shows variation in the lengthwise pressure readings, indicating a non-zero pressure gradient. In this configuration, the pressure coefficient changes by as much as 1322 counts, with a large pressure decrease at port 5. As the flap moves in the downward direction, the pressure gradient improves, seen in Table 3 with an essentially zero pressure gradient being reached at the five degree downward position.

Table 3: Ground Plane Pressures at Various Flap Positions

Flap Pos.	P1 C_p	P2 C_p	P3 C_p	P4 C_p	P5 C_p
-5 Degrees	-0.0100	0.001	-0.008	-0.017	-0.1312
1 Degree	-0.092	-0.024	-0.093	-0.071	-0.110
2 Degrees	-0.072	-0.041	-0.077	-0.059	-0.100
5 Degrees	-0.029	-0.007	-0.012	-0.008	-0.004

At 5 degrees down, while the pressures downstream of the leading port are a little higher, they are much more consistent between P2 and P5, with a maximum change in pressure coefficient being 80 counts, which cover almost the entire length. For this reason it was chosen that all testing would be performed with a 5 degree downward position.

The stethoscope results indicated that laminar flow was only achieved at half plane length for 10 m/s, and at full plane length at 5 m/s, in line with our theoretical Reynolds number calculations. However, these results also indicated proper orientation of the trailing edge flap and the design of the ground plane as a whole to prevent leading edge separation. In Figure 23 the acoustic waveform graphs for each test speed are shown, measured at 0.5 meters from the leading edge. For the 5, 10, 20 and 30 m/s cases the probe was moved from freestream measurement to the ground plane boundary layer, at roughly 30 seconds. By looking at the 5 and 10 m/s velocity cases it can be seen that the boundary layer of the ground plane is laminar. In comparison to the freestream readings, the magnitude of the sound waves did not increase when the probe was moved to the surface of the ground plane, suggesting that the boundary layer shares the same laminar flow properties as the freestream flow. On the other hand, the 20 and 30 m/s velocity cases do not show this same trend. When the probe is moved into the ground plane's boundary layer, the magnitude of the graphs jumps dramatically, an indication of turbulent flow.

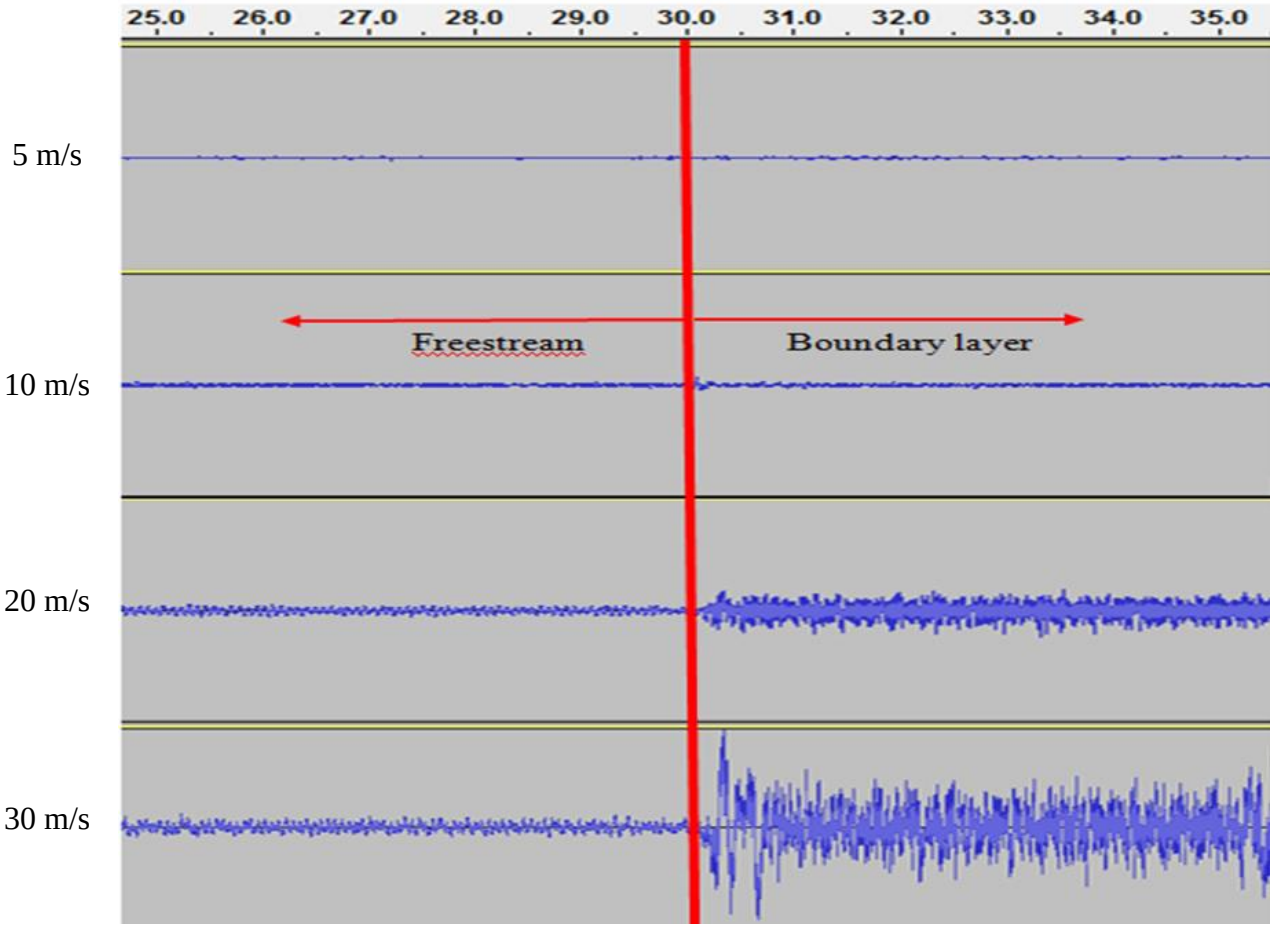

Figure 23: Boundary Layer Stethoscope Waveforms

7.1 Model Base Pressure

7.1.1 Non-tabbed Model

Pressure measurements along both the spanwise and normal directions on the model base give insight into the effectiveness of tabs as a drag reduction device when the model, a bluff body, is operating in ground effect. The graphs in this section will show the trends in base pressure as a function of ground clearance height, from model base pressures with no ground plane present to model base pressures with ground clearances of H/h = 0.25.

Figure 24 shows the normal pressure distribution for 10 m/s. The no ground plane case data is consistent with previous test results, and shows two valleys in the pressure data, an indication of vortex shedding. Both the magnitude and shape of the no plane pressure distribution are similar to Barker's[7] results, indicating a good baseline configuration to which the ground plane cases can be compared to.

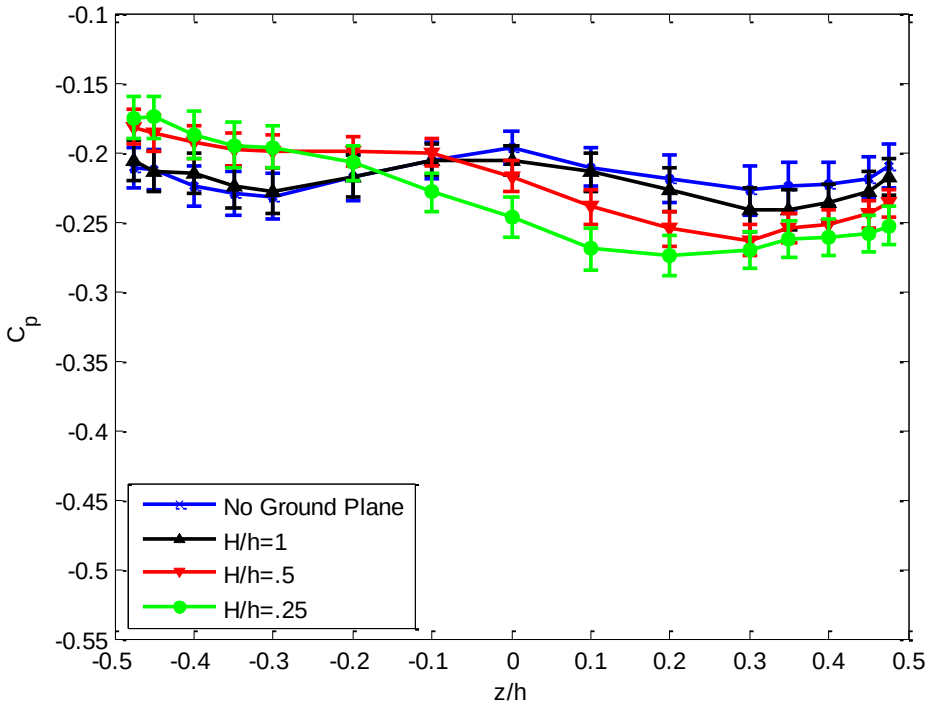

Figure 24: Normal Direction Base C_p for Untabbed Model at 10 m/s

Once the ground plane is introduced to a clearance of H/h = 1, its effects are barely noticeable. The pressure distribution of both the no ground plane and non-dimensional clearance height of H/h = 1 fall almost on top of each other, and well within the error bars of each distribution. However, as the ground plane is lowered to H/h = 0.5, its effects become noticeable. The base pressure on the ground plane side begins to rise, while the pressure on the opposite end, the unbounded side furthest from the ground plane, begins

to decrease. This trend continues at the lowest ground plane clearance of H/h = 0.25, where the bounded side pressure coefficient rises to -0.175, but the unbounded plane side of the bluff body experiences a pressure drop to -0.250.

Figure 25 shows the spanwise direction pressure readings for the non-tabbed 10 m/s test. Again, both the no ground plane and H/h = 1 case show the same trend, and the ground plane does not seem to have any influence at such a large clearance. Dips on each side of the base plate indicate vortex shedding is occurring, with a pressure increase towards the middle of the plate. Once the clearance is lowered, the overall spanwise base

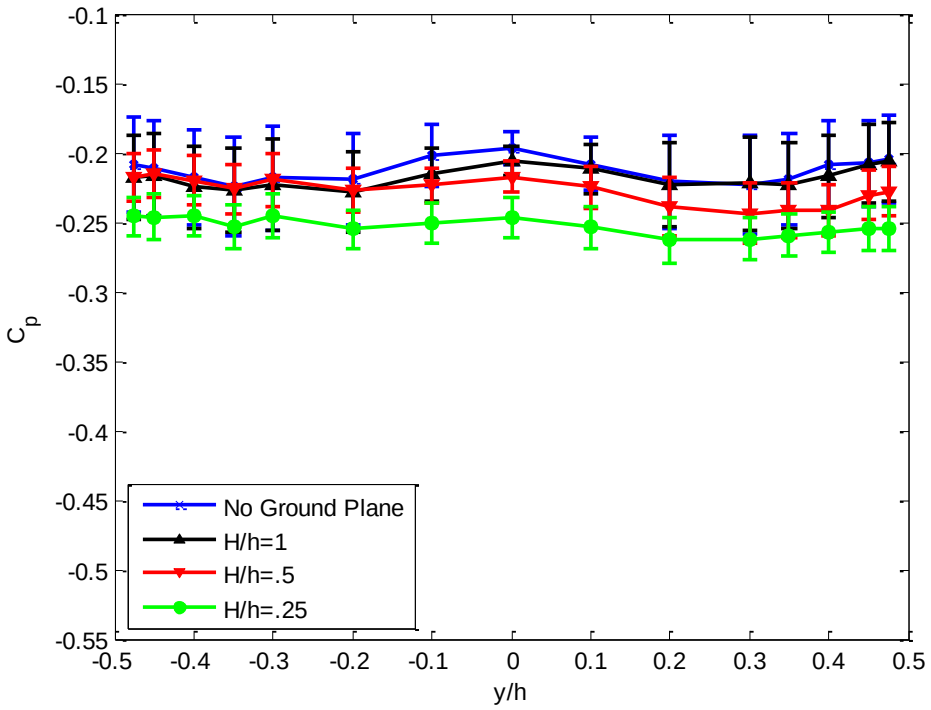

Figure 25: Spanwise Base Pressure Coefficient for Untabbed Model at 10 m/s

pressure begins to drop. At the lowest clearance of H/h = 0.25 the dips in pressure at each side have diminished, with the normal direction C_P's hovering around -0.25.

Overall, it can be seen that as the ground plane is moved closer to the model the pressures nearest the ground seem to drop, while the unbounded flow side experiences a rise in pressures. It should also be noted that for the 10 m/s case the error bars indicate much more fluctuation in pressures near the edges of the model, where the vortex shedding is occurring, and show steadier, more consistent readings near the middle of the base plate.

At 20 m/s tunnel velocity the trend is similar to the 10 m/s case, but the ground interaction has a greater influence at the H/h = 1 case. Figure 26 shows this effect in the normal C_p distribution, and it can be seen that with the ground plane in the tunnel at the largest clearance of H/h = 1.0, the pressure on the ground plane side has already begun to increase and near the unbounded side the pressure has dropped compared to the no ground plane case.

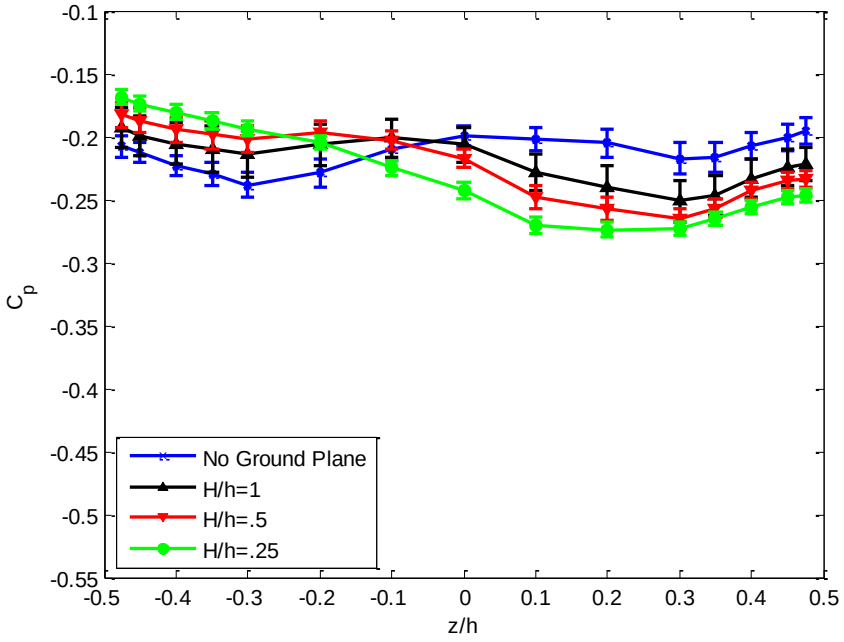

Figure 26: Normal Base Pressure Coefficient for Untabbed Model at 20 m/s

Additionally, as the ground clearance is further decreased, the pressure readings on the bounded flow side remain about constant across the gap clearances, with the variation not occurring until the 5th pressure port in from the edge.

The spanwise direction pressure readings at 20 m/s paint a slightly different picture than those of the 10 m/s data. Figure 27 shows that with the ground plane inserted to a height of H/h = 1 from the model, the flow is already affected, with the pressures being slightly lower than the no ground plane case, with a maximum difference in C_p of 0.10. As the ground clearance continues to decrease, the spanwise pressure trends continue, with the Cp's dropping to an average value of -0.249.

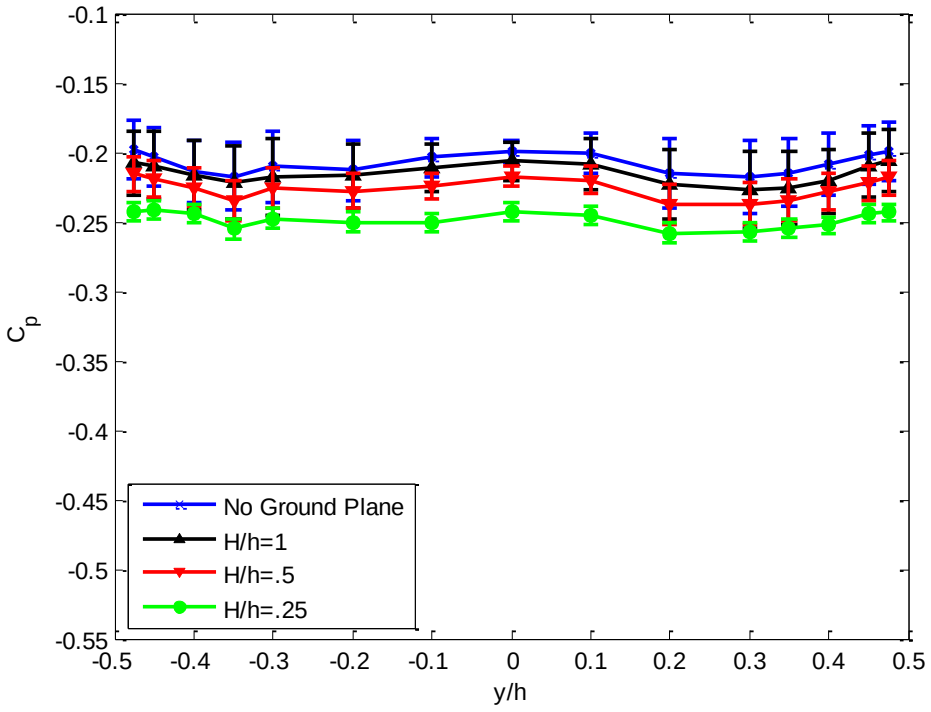

Figure 27: Spanwise Base Pressure Coefficient for Untabbed Model at 20 m/s

For all 20 m/s data the error bars are much smaller than those of the 10 m/s test case, indicating steadier, more accurate data. It can still be seen that the variation in Cp's

near the edges of the baseplate of the model are greater than at the interior pressure ports, suggesting that the lager error bars in the 10 m/s data are not from volatility of the flow, but that measurement error is greater at the slower speeds, caused by the lower dynamic pressure.

The third and final test speed was 30 m/s and base plate pressure readings at this velocity agree with the results observed at the lower speeds. Again in the normal direction, shown in Figure 28, the ground plane at a clearance of H/h = 1 begins to affect the base pressure, raising the pressure on the ground plane side. However, it can be

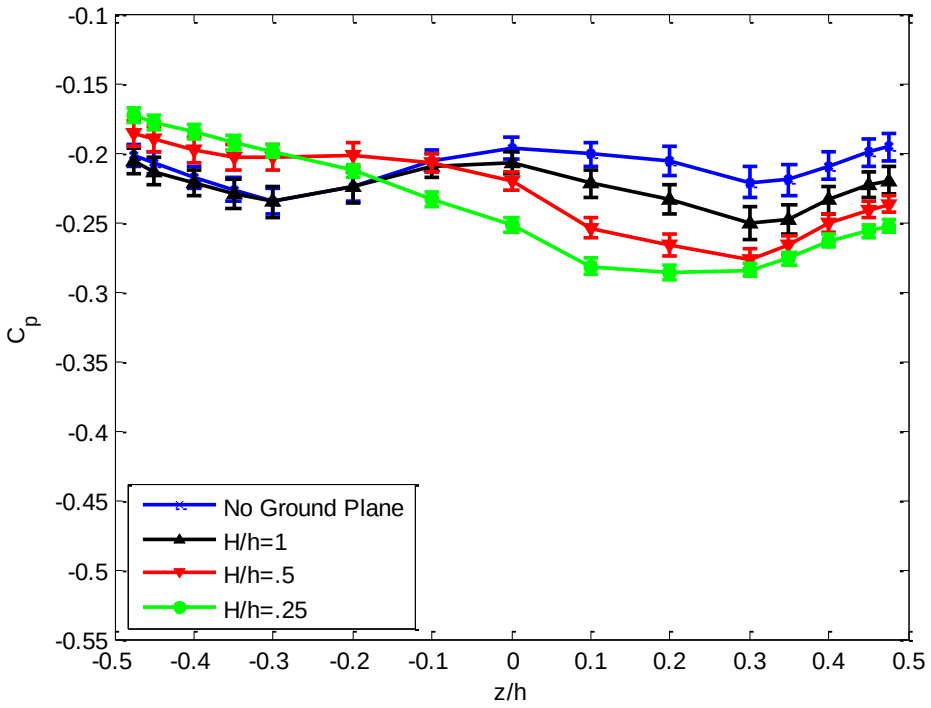

Figure 28: Normal Base Pressure Coefficient for Untabbed Model at 30 m/s

noticed that there is no statistical difference in pressures at the bounded flow side, with the C_p's matching well with the no plane case. As soon as the ground plane is lowered to

H/h = 0.5 however, its effects become clear, and just as at the previous two speeds, the pressure on the bounded side increases, while the unbounded side sees lower pressures.

As for the spanwise pressures, depicted in Figure 29, it can again be seen that a decrease in ground clearance leads to a decrease in base normal direction pressures, with the no plane case having an average CP of -0.214 while the H/h = 0.25 ground plane case has an average C_P across the ports of -0.260.

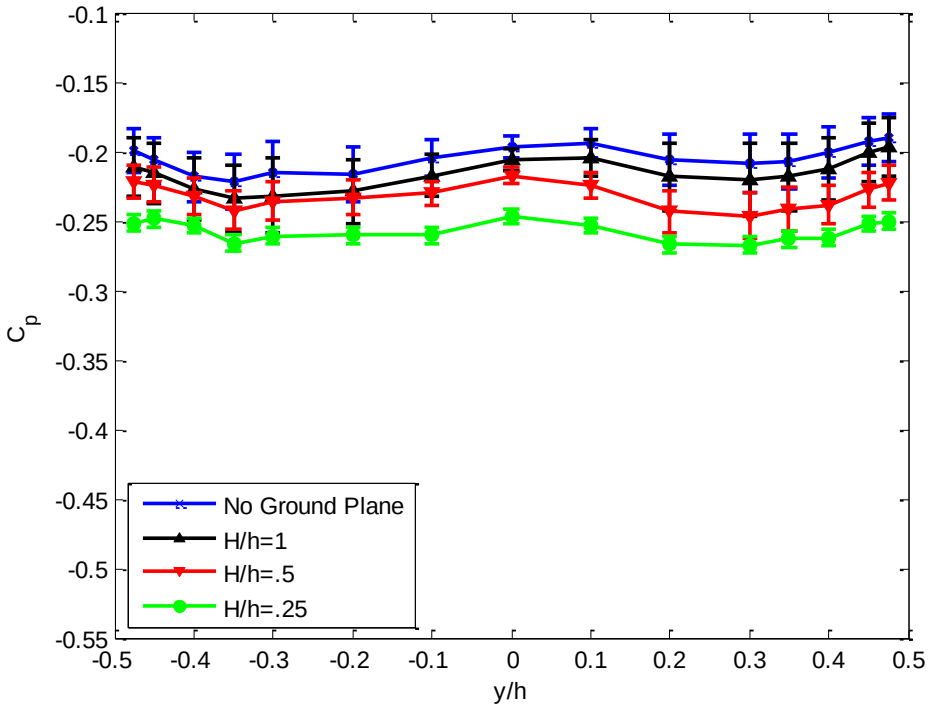

Figure 29: Spanwise Base Pressure Coefficient for Non-tabbed Model at 30 m/s

Pressure coefficients for each tunnel velocity, grouped by ground clearance, are shown in Figure 30 below. This data gives some insight into how bounded flow characteristics are affected by velocity for constant ground clearances. There is very little variation in base pressure in between speeds, but the introduction of the ground plane has a clear effect. In the top left corner of the figure is the baseline normal Cp graph for the

model, in which the ground plane is removed from the tunnel. At all speeds, the pressure distribution seems to be the same, with signs of vortices on each edge of the model. Once the ground plane is introduced with a clearance of H/h = 1, no clear effects are yet seen either, with the distribution being similar in form to the no plane case. At the two lowest ground clearances the effect of the ground plane is evident, with the pressures decreasing on the unbounded flow side, while the bounded side experiences a pressure rise, up to a value of -0.173 C_p for the lowest gap clearance.

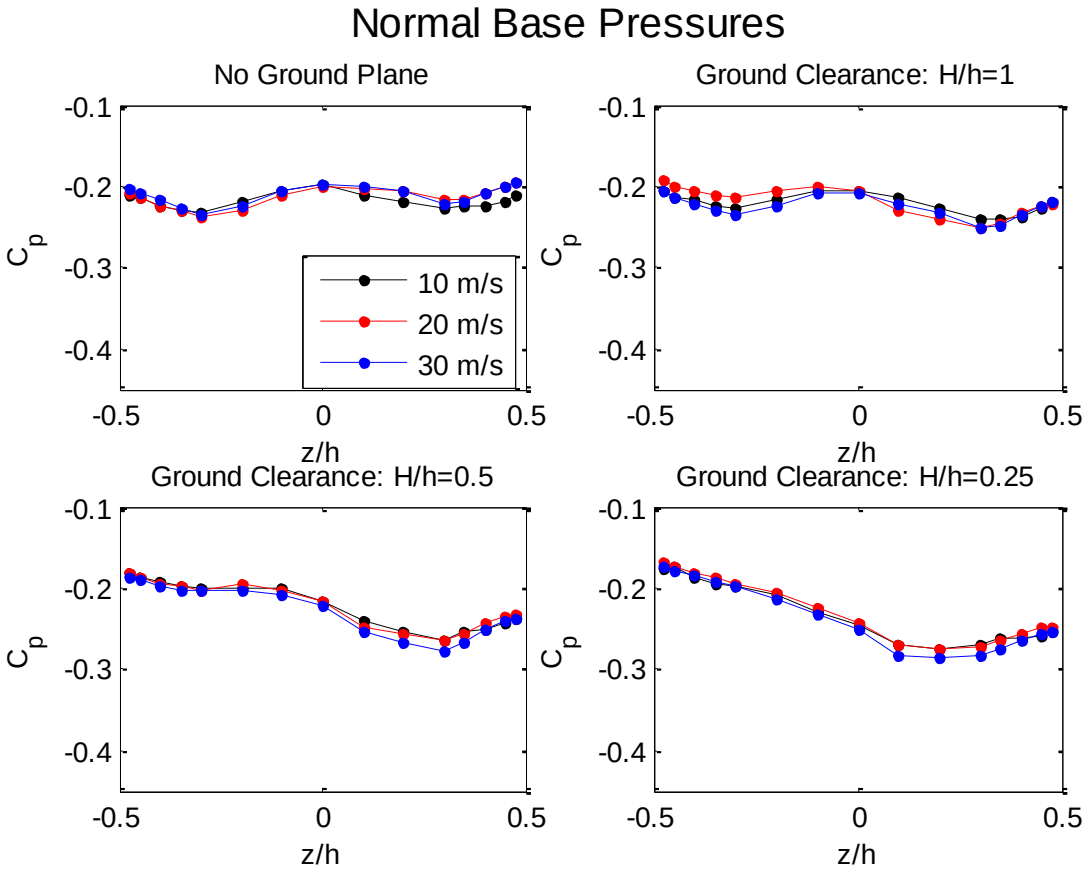

Figure 30: Normal Direction Cp for Non-tabbed Model by Ground Clearance

The spanwise direction of C_p shows a similar trend, as seen in Figure 31. For the no plane case, the pressure distribution is similar across all speeds, and the vortex shedding

dips can again be seen along each edge of the base. There is little to no change of pressure distribution with the ground plane at the largest tested clearance, but once the gap height is lowered to H/h = 0.5, the pressures begin to drop uniformly across the spanwise direction. At the lowest clearance, the pressures fall even further, and the signs of vortex shedding on either of the model are less evident than in the no ground plane interaction case.

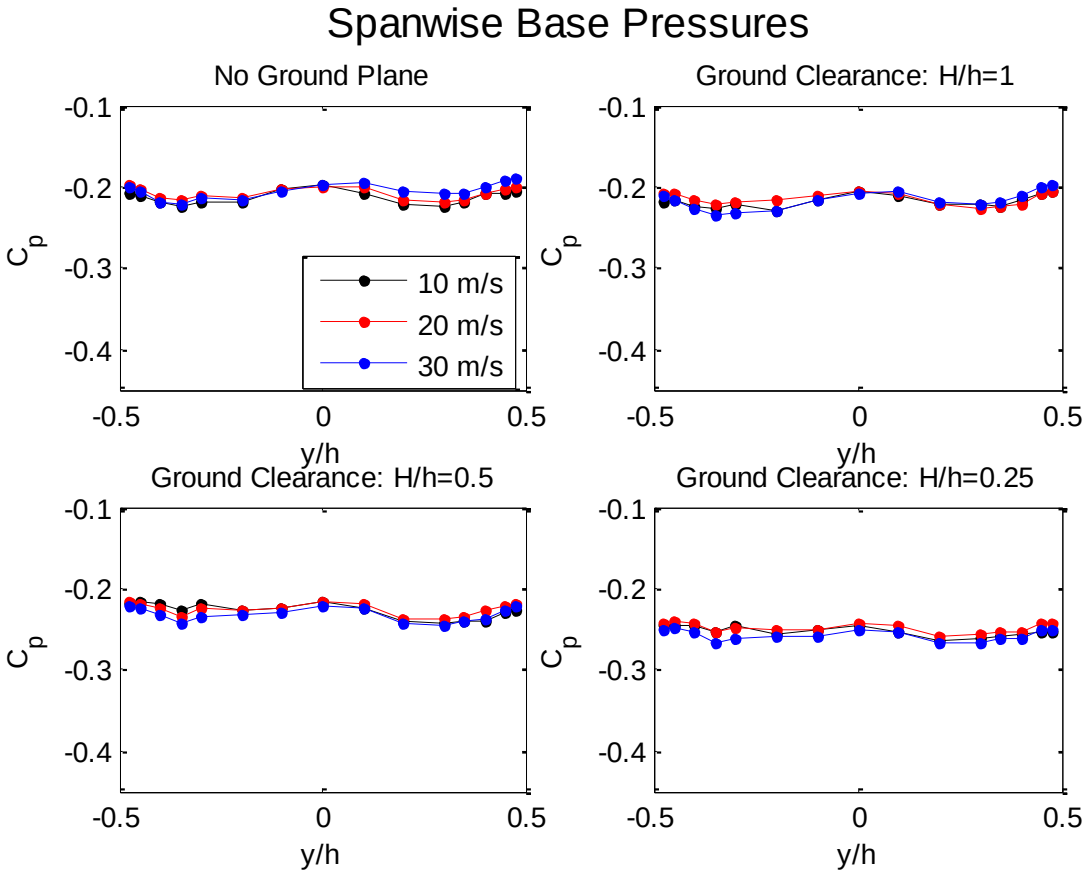

Figure 31: Spanwise Cp for Non-tabbed Model by Ground Clearance

Overall, the spanwise Cp's, averaged out across the entire base, are -0.25, -0.25, -0.26 for the 10, 20 and 30 m/s test cases, respectively, with the ground gap height at a

ratio of 0.25. With no ground plane, the Cp values are -0.21, for all respective test speeds, and the vortex shedding is much more evident.

7.1.2 Tabbed Model

The tabbed base plate overall showed the same trends as the non-tabbed base plate, but showed lower pressures across all speeds and ground clearances in general. For each tabbed test case, the model was kept in the same orientation in the tunnel, and when the tabbed base plate was installed, care was taken to ensure symmetric installation, guaranteeing symmetric vortex shedding results for the no plane testing.

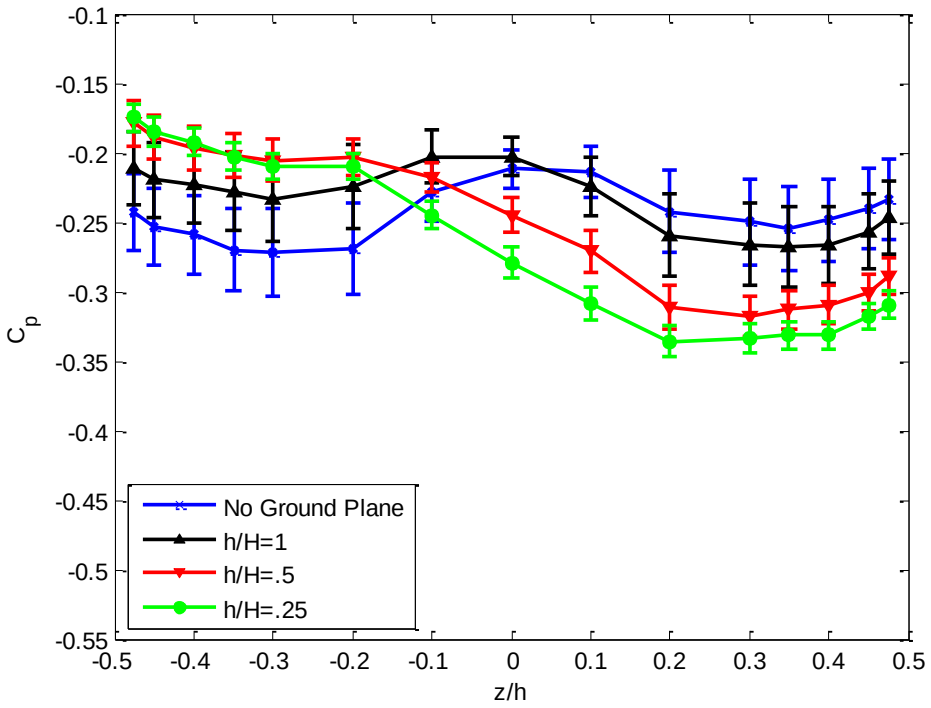

Figure 32: Normal Base Pressure Coefficient for Tabbed Model at 10 m/s

Figure 32 shows the normal pressure coefficients for the tabbed base plate 10 m/s test case. A similar trend is evident: introduction of the ground plane decreases pressures on the unbounded flow side of the model while increasing pressure on the bounded flow

side. In fact, this trend remains similar for all test speeds, as can be seen in Figure 33 and Figure 34, which show data from the 20 and 30 m/s cases, respectively. Once the ground plane is introduced, it can be seen that the pressure coefficients on the unbounded flow side drop, while the pressures near the ground plane rise. Interestingly, the pressures right near the bounded side edge do not seem to change much at the two lowest ground clearances, as the C_p values stay steady across all ground clearances. In fact, the six ports closest to the ground side edge have negligible difference at the 20 and 30 m/s test cases, indicating that flow conditions around the edge are similar, even at H/h = 1 ground clearance.

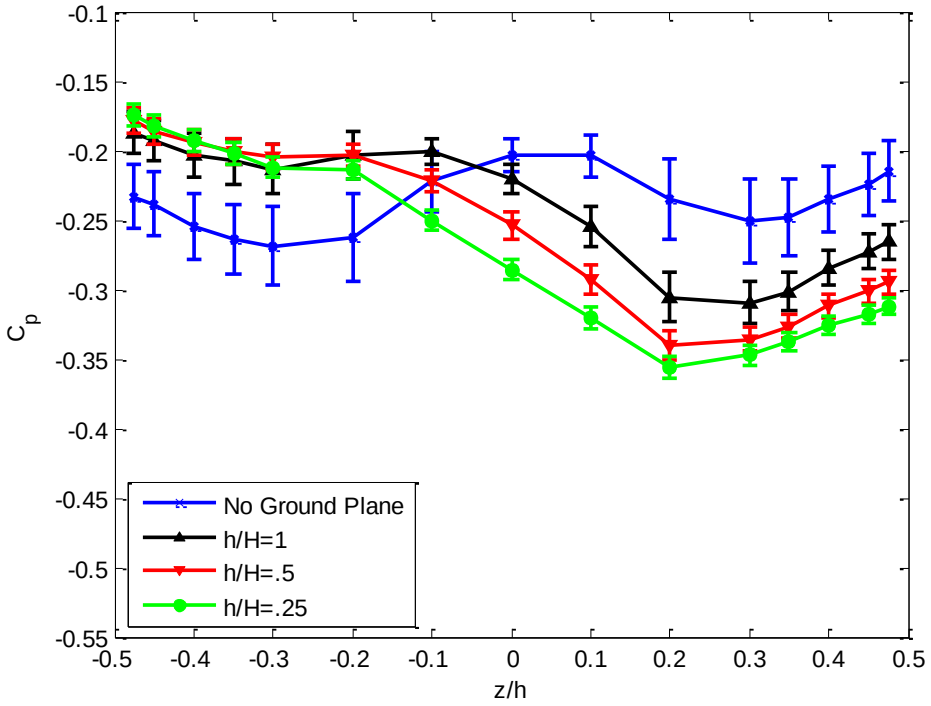

Figure 33: Normal Base Pressure Coefficient for Tabbed Model at 20 m/s

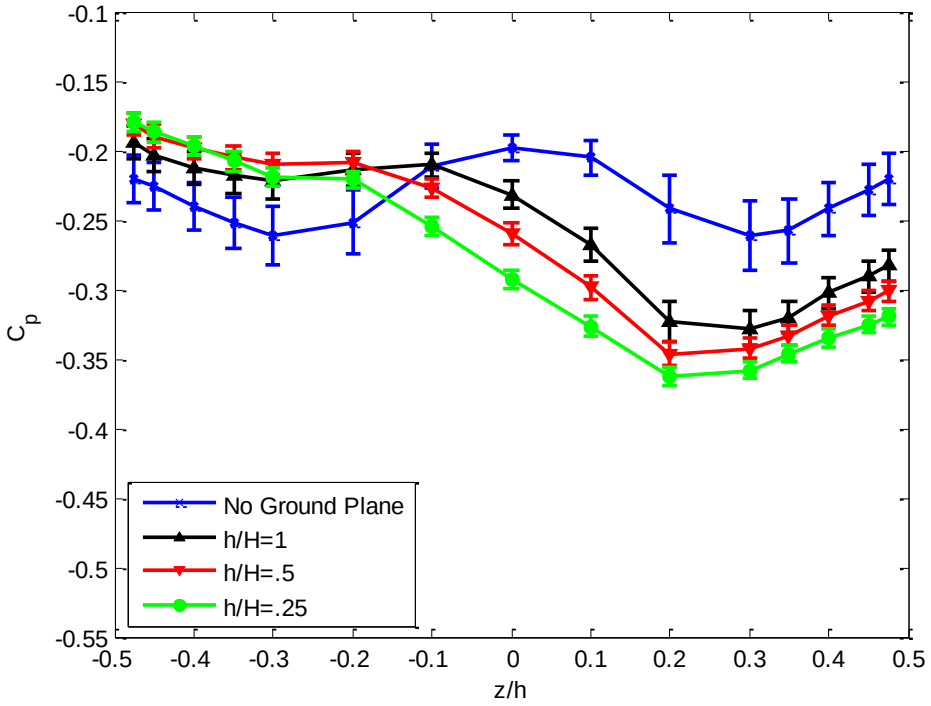

Figure 34: Normal Base Pressure Coefficient for Tabbed Model at 30 m/s

However, it can be seen that as the ground plane is moved closer to the model, the vortex shedding on the unbounded side gets stronger and wider, with effects reaching well across the halfway point of the base plate, with the pressure port at z/h = -0.1 even seeing the effect.

Across the spanwise direction of the tabbed base plate the interaction of the ground plane again has a strong effect, yet similar to the non-tabbed version, evidenced in Figure 35, which displays the spanwise pressure coefficients at the 10 m/s test case.

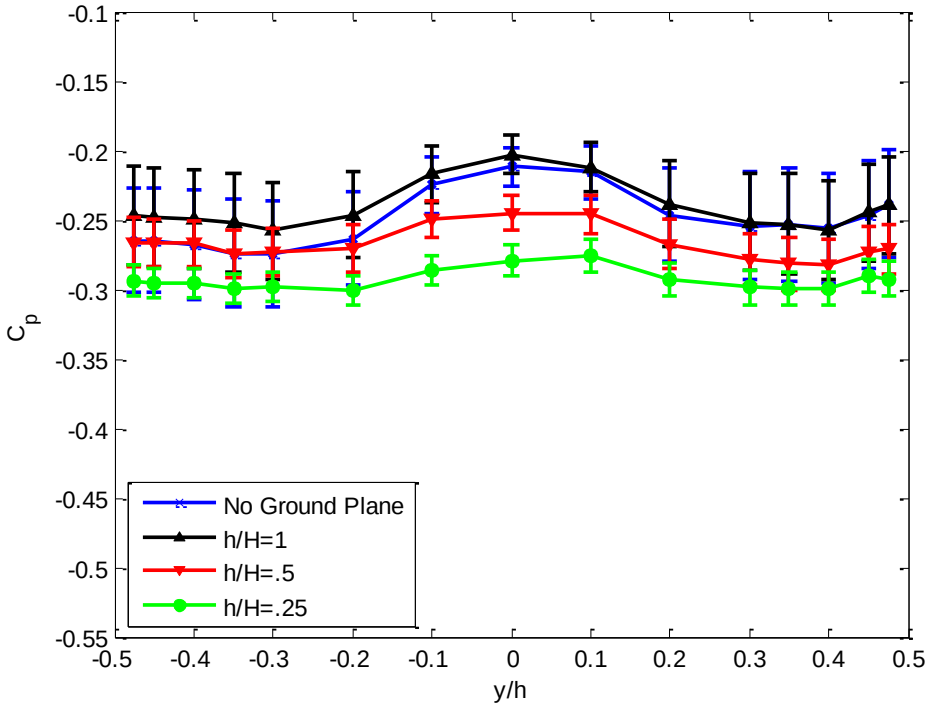

Figure 35: Spanwise Base Pressure Coefficient for Tabbed Model at 10 m/s

As the ground plane is moved nearer the model, the pressure coefficient decreases, mainly due to the stronger, wider vortex shedding that is occurring along the unbounded side. Additionally, the vortex shedding in the normal direction is minimized as the ground clearance decreases. As can be seen at all speeds, the dips on each side of center with no ground plane present are a sign of vortex shedding. These dips occur even though the model has tabs, showing the lack of effectiveness the tabs have in attenuating the vortex shedding, which will be discussed in detail later on. Most importantly, these dips in pressure coefficient weaken as the ground clearance is lowered, a sign that the spanwise vortex shedding is being overpowered by the stronger vortex created on the unbounded side of the model. Figure 36 shows the base pressures for the tabbed model at 20 m/s, in the spanwise direction.

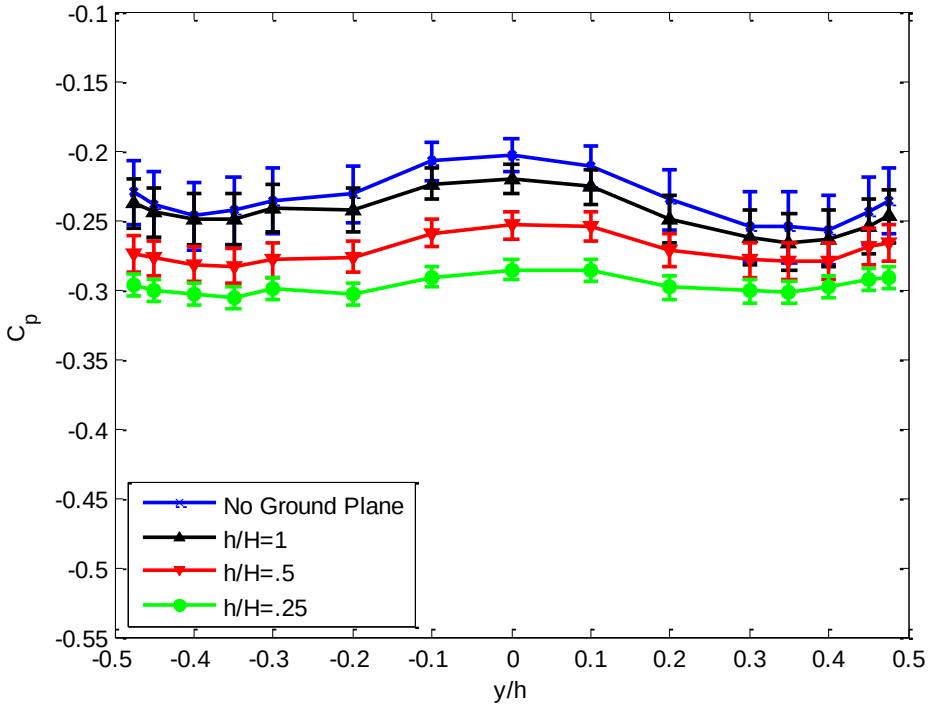

Figure 36: Spanwise Base Pressure Coefficient for Tabbed Model at 20 m/s

Again, it can be seen that the tabbed model displays lower baseline pressure when there is no ground plane present as compared to the non-tabbed version. Interestingly, the vortex shedding seems to be noticeably stronger for the tabbed case as well, with deeper drops in pressure near the edges of the model base when the ground plane isn't present. Comparisons and analysis of this difference will be presented in the discussion section.

At the 30 m/s test case, the spanwise pressure coefficient drops 0.066 at H/h = 0.25 ground clearance compared to the no ground plane case. Again, the trend in pressures is similar in that the spanwise pressures decrease as the ground clearance decreases, with the pressures becoming much more uniform across the length of the normal direction, as can be seen in Figure 37.

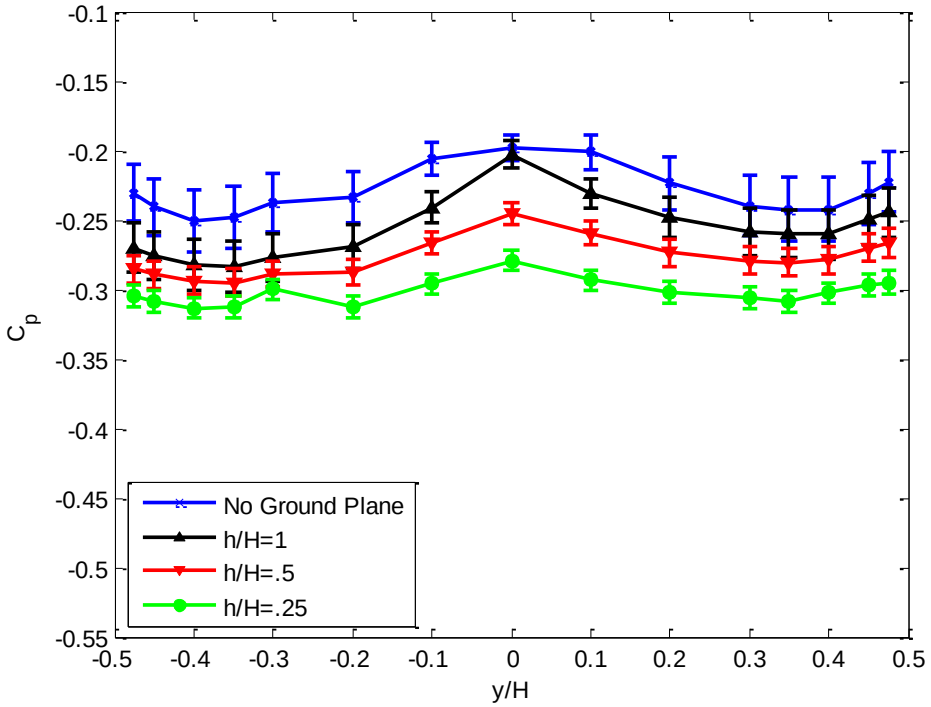

Figure 37: Spanwise Base Pressure Coefficient for Tabbed Model at 30 m/s

For the spanwise direction, an overall trend can be seen: as the ground clearance is decreased, the pressure readings also decrease. Detailed explanations for this will be discussed in the next section, but, in short the ground interaction causes a vortex that forms further downstream.

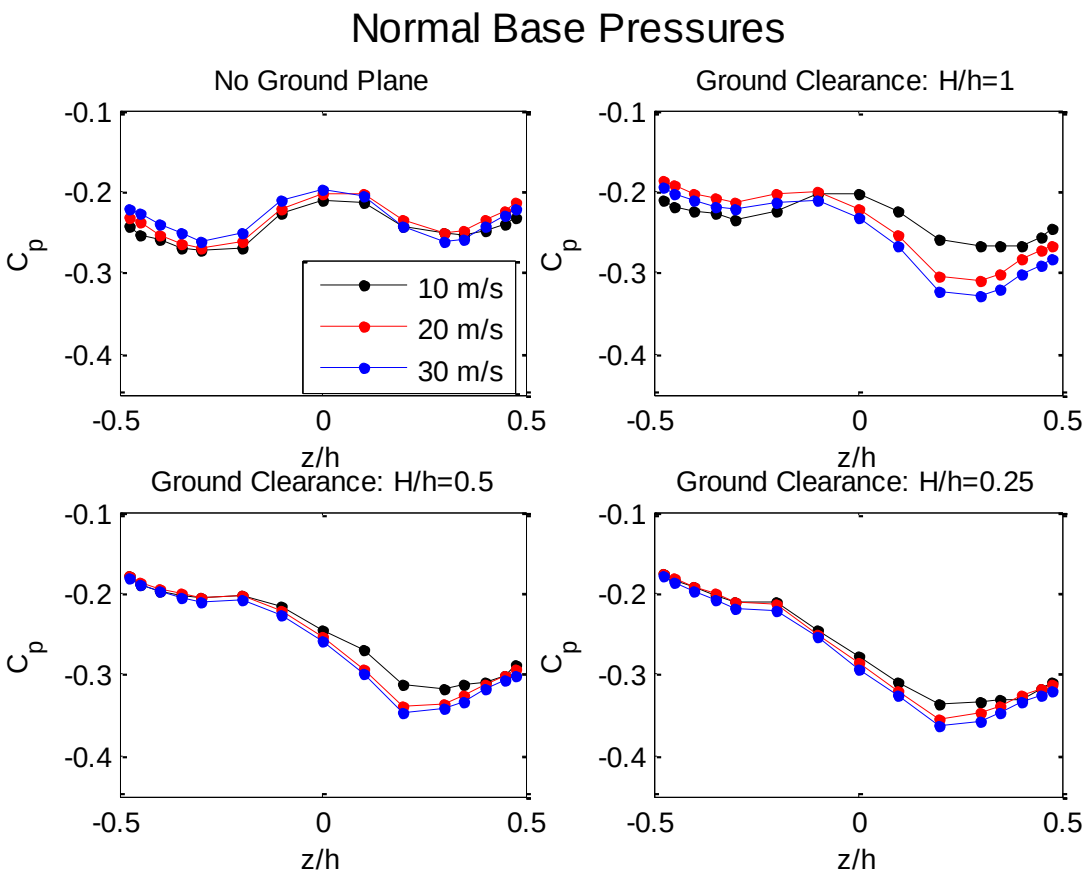

Figure 38: Tabbed Model Normal Base Pressure by Variation in Ground Clearance

Figure 38 displays the normal pressure coefficients for each ground height clearance, graphed by test velocity, for the tabbed model. While similar to the non-tabbed model results, there is one key difference worth noting. For the 10 m/s test case, the pressure readings on the bottom of the model, the bounded side, are systematically higher than the 20 and 30 m/s. However, with no ground plane all three test speeds show similar pressure coefficients across the normal direction.

The spanwise direction results are shown in Figure 39. Again, there are slight variances compared to the non-tabbed case. With no ground plane, the 10 m/s case shows a lower base pressure coefficient on the positive y side of the base. However, this is most

likely caused by a slight asymmetry in the tabbed base plate, and does not dictate a real phenomenon. Theoretically, the graphs should be symmetric about the centerline of the model, with pressure coefficients being mirrored on each side.

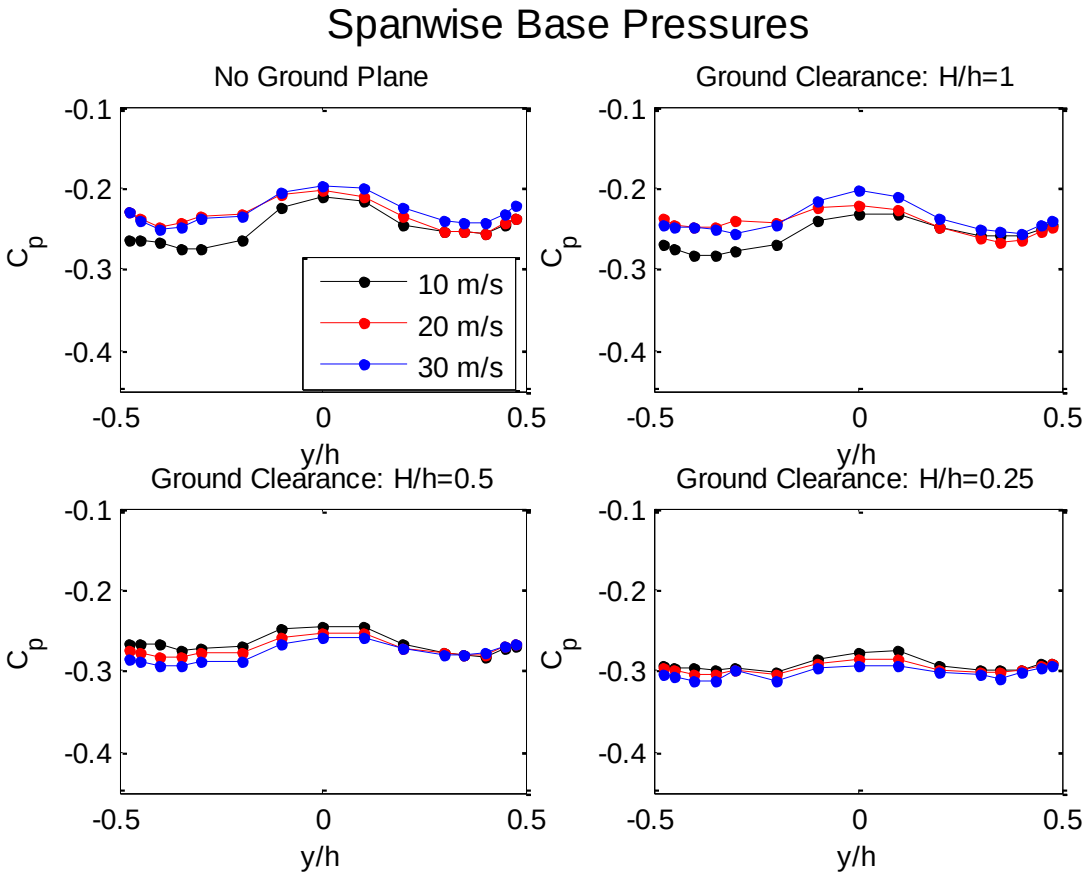

Figure 39: Tabbed Model Spanwise Base Pressure by Variation in Ground Clearance

Due to the installation method of the tabbed base plate however, small variances in symmetry can be expected, as it was found during testing that even minimal changes to the base plate location can lead to large changes in data. Additionally, the system to adjust model yaw could not be computer controlled, resulting in variances by as much as .1 degrees, adding to the differences from a perfectly symmetrical pressure distribution.

Overall, the raw pressure data shows that the ground plane influences the flow around the bluff body trailing edge in two ways. On the base side nearest the ground plane, in the normal direction, which experiences the largest portion of bounded aerodynamics, the pressure dip actually increases as the ground clearance is decreased, with the vortex shedding on that edge being reduced dramatically. However, on the opposite side of the base, furthest from the ground plane, there is a large decrease in pressure as the ground clearance decreases. As the gap clearance is lowered, the vortex over the unbounded edge becomes stronger and deeper in nature, affecting the ports in the normal direction. Because of this, the pressures across the spanwise direction of the bluff body are shown to uniformly decrease with decreasing ground height clearance.

7.2 Drag Coefficient

Data shown in Figure 40 shows the drag coefficient for the non-tabbed baseplate model, at each ground clearance and Reynolds Number. These results are in stark contrast to previous work done in the Cal Poly wind tunnel, in which large increases in drag coefficient were seen as the tunnel speed was increased from 10 m/s to 20 m/s in both Barker[7] and Pinn's[5] experiments. In this experiment, the data suggest that the drag coefficient remains roughly constant across Reynolds number, with only slight variations occurring between each test case. In fact, a much larger variation in drag coefficient is caused by the ground clearance height, with the sting balance data showing a noticeable decrease in drag force due to the interaction of the ground plane. Interestingly, the data shows that for decreasing ground clearances, the drag coefficient will decrease up to a certain height, often referred to as a critical gap height, and then actually begins to increase for lower gap clearances.

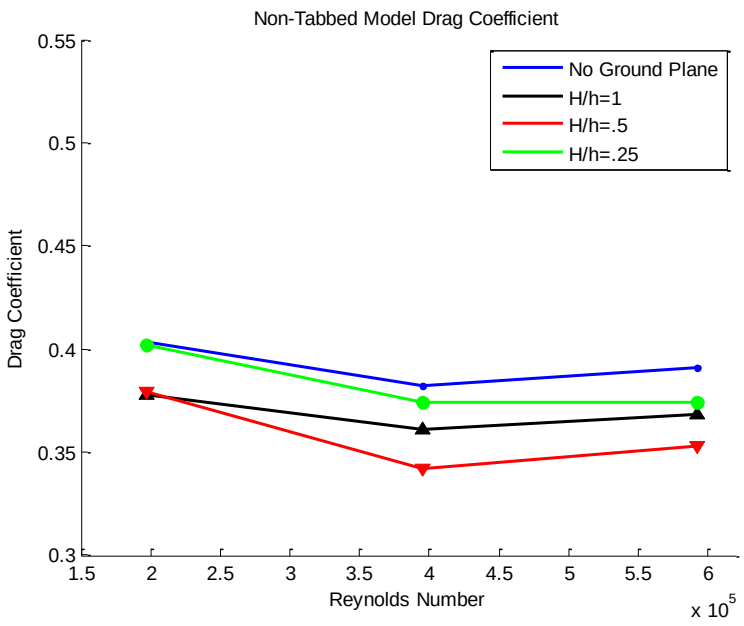

Figure 40: Drag Coefficient for the No Tabs Model

In this present data, it can be see that the critical gap height occurs between H/h = 0.25 and H/h = 0.5. This same trend is seen with the tabbed version of the model, with the drag data presented in Figure 41.

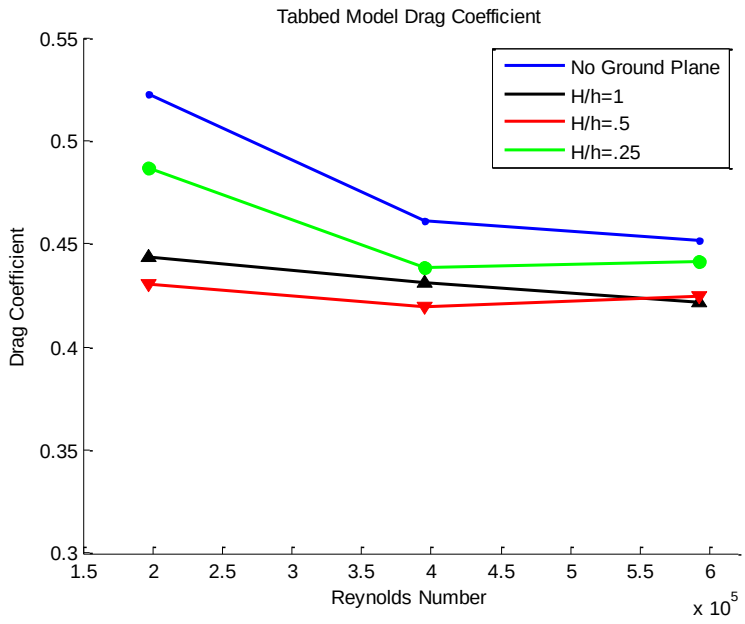

Figure 41: Drag Coefficient for the Tabbed Model

Again, for the tabbed model in Figure 41, drag coefficient decreases as the ground clearance decreases, up until the 0.25h ground plane case. However, at this lowest clearance, the drag coefficient rises above the 0.5h and 1h clearance test cases, but does not surpass the no ground plane baseline case. Additionally, it can be observed that the drag coefficient is generally higher for the tabbed model than the non-tabbed model.

Table 4: Drag Coefficient Comparison

	No Ground Plane			h/H=1			h/H=0.5			h/H=0.25		
Velocity	**10**	**20**	**30**	**10**	**20**	**30**	**10**	**20**	**30**	**10**	**20**	**30**
No Tabs ΔCd	-	-.021	-.012	-.025	-.042	-.025	-.024	-.061	-.050	-.001	-.029	-.029
Tabs ΔCd	.119	.058	.048	.040	.028	.018	.027	.016	.021	.084	.036	.038

Table 4 summarizes the drag coefficient change for each test case compared to a the non-tabbed, no ground plane 10 m/s test case, which will be deemed the baseline scenario. As

shown, all drag coefficients of the tabbed model are larger than the non-tabbed counterpart, agreeing with results obtained by Barker[7] in his experiment. In fact, the tabbed version, at a maximum, adds 119 counts of drag at the 10 m/s no ground plane test case, the largest difference of any velocity and test configuration.

The sting balance results suggest two primary conclusions: that drag coefficient stays fairly constant with Reynolds Number, and second, that drag force is influenced by ground clearance, with the drag actually decreasing over the baseline no-ground plane interaction case.

8. DISCUSSION

This section will focus on explaining the data shown in the previous section. Additionally, it will look at the data in different lights, making comparisons between cases, analyzing trends, and investigating relationships not immediately clear from the data presented in the results section.

8.1 Variances in Error

The first thing to note of the results is the differences in error bars for each of the pressure port readings, and this difference must be addressed before validating any other results. At the 10 m/s test cases, the graphs show a large range of error; so much in fact that the results of the error calculations lead to a weak confidence that there is a difference in pressure readings between each ground clearance, due to the overlapping of the error bars between each test cases. For the 20 and 30 m/s wind tunnel speeds it can be seen that the error significantly decreases for the pressure readings, generating substantial confidence that the results between each ground clearance are statistically different. Table 5 shows the pressure errors for the tabbed model at each pressure port, in the normal direction for just the bounded half of the model, with no ground plane present.

Table 5: Pressure Errors

Port Location (y/h)	-.48	-.45	-.40	-.35	-.30	-.20	-.20	0.00
10 m/s	±0.037	±0.038	±0.039	±0.039	±.038	±0.034	±0.021	±.0140
20 m/s	±0.023	±0.024	±0.025	±0.024	±0.023	±0.020	±0.013	±0.012
30 m/s	±0.020	±0.021	±0.022	±0.021	±0.021	±0.018	±0.011	±0.009

The main trend in this data is the much larger errors near the edges of the model as compared to the middle of the model. This, however, can be expected due to the nature of vortex shedding: near the trailing edge of the model the flow field is in a constant state of cyclical vortices, so the pressure readings can be expected to fluctuate a lot more than at the center of the base plate, where the effect of the vortex shedding is less pronounced. However, a more interesting finding is the much smaller errors at lower ground clearances, suggesting that there is less variation in pressure readings as the model moves closer to the ground plane. As the graphs in the results sections show, for each test speed, and for each model configuration, the 0.25h ground clearance displays the smallest error bars in each case. The smaller errors at the lower ground clearances seem to suggest that there is less fluctuation in pressure readings caused by a less volatile vortex, compared to the higher errors seen in the pressure readings at the upper, unbounded surface.

8.2 Drag Measurement

The measured sting balance drag is consistent with results seen in similar testing. In Figure 42 below, Bearman's[14] results for drag coefficient are shown. As can be seen, at large ground clearances there is almost no change in drag coefficient, while at the low ground clearances drag coefficient is parabolic in nature.

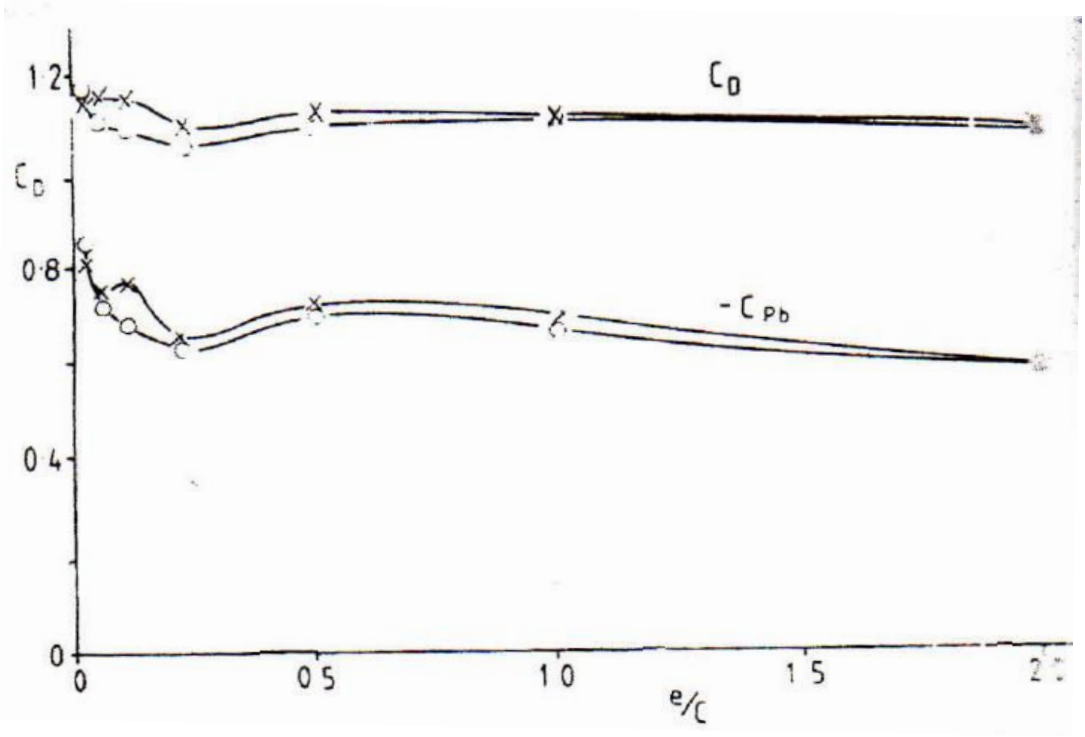

Figure 42: Bearman's[14] Drag Coefficient Results

Likewise, when the drag data from this experiment is shown in relation to ground clearance, that same parabolic shape is present. Although the drag coefficients of Bearman's results are larger, likely due to his model having a flat front face compared to the rounded face if the model in the current experiment, the trend in drag coefficient is similar. In Bearman's test, he used the length of the model as his reference dimension to calculate ground clearance, while the height of the model was used in testing performed for this thesis. Once this difference is adjusted for, the clearances seen in this test would be well on the left side of Bearman's data, in the 0.1 to 0.4 range.

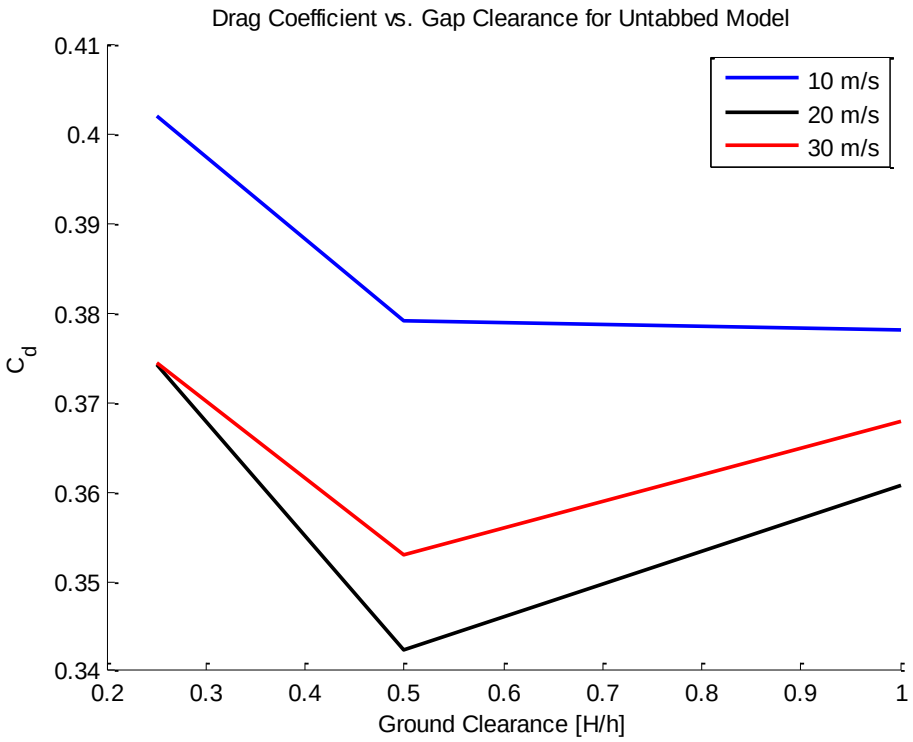

Figure 43: Drag Coefficient by Ground Clearance

Most important to note are the small changes that occur in drag coefficient. At 20 m/s, which saw the greatest disparity in drag, the largest measured difference in C_d was 0.021. Compare this to the error involved when calculating the drag coefficient whose values range in the 0.015 area, shown in the appendix, and it can be said there is no significant change in drag coefficient with variation in Reynolds Number.

8.3 Base Pressure

The baseline non-tabbed, no ground plane base pressure readings agree with experiments performed by Barker[7], and indicate a valid baseline case from which to make comparisons. Barker found that the tabbed model had an increase in C_d 4.9%, 5.1%, and 2.1% at the 10, 20 and 30 m/s test speeds, respectively. In the present experiment, it was seen that drag is also increased with the addition of trailing edge tabs, but as much as

15.5% at the 30 m/s test case. These results confirm that the addition of tab devices on the trailing edge of the bluff body do not decrease overall body drag as reported by Pinn, and in fact cause a significant increase in overall drag.

When the ground plane is introduced into the test section, the overall base pressures begin to drop. Figure 44, which shows the average base pressure coefficient for the non-tabbed model, shows that the overall base pressure coefficient, averaged across all 30 recorded ports, drops 0.027, 0.028 and 0.038 for the 10, 20 and 30 m/s test cases, respectively, in comparison to the no ground plane test case.

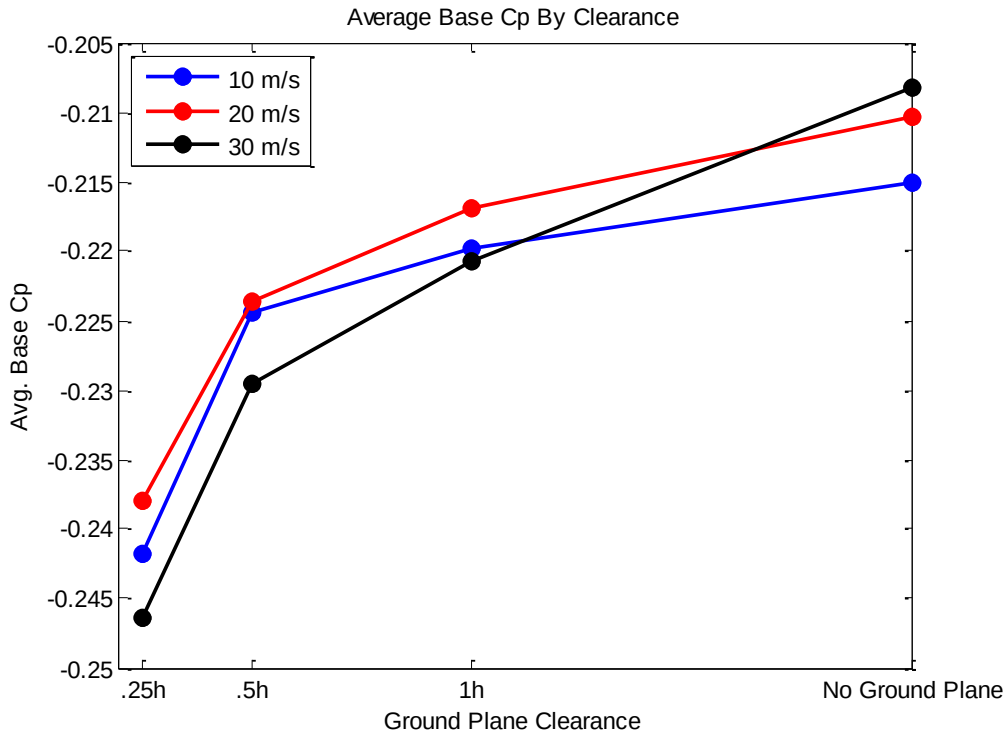

Figure 44: Average Base Pressure for Non-tabbed Model at Each Ground Clearance

Likewise, for the tabbed model case, the averaged base pressure coefficient can be seen in Figure 45 below, which shows a similar decrease in base pressure with decreasing ground plane clearance, with the single outlier of the no ground plane, 10 m/s case.

However, as discussed with the original results, this drop in pressure can be attributed to the slightly asymmetrical 10 m/s normal pressure distribution shown in Figure 45, most likely caused by a slight offset on the back plate installation.

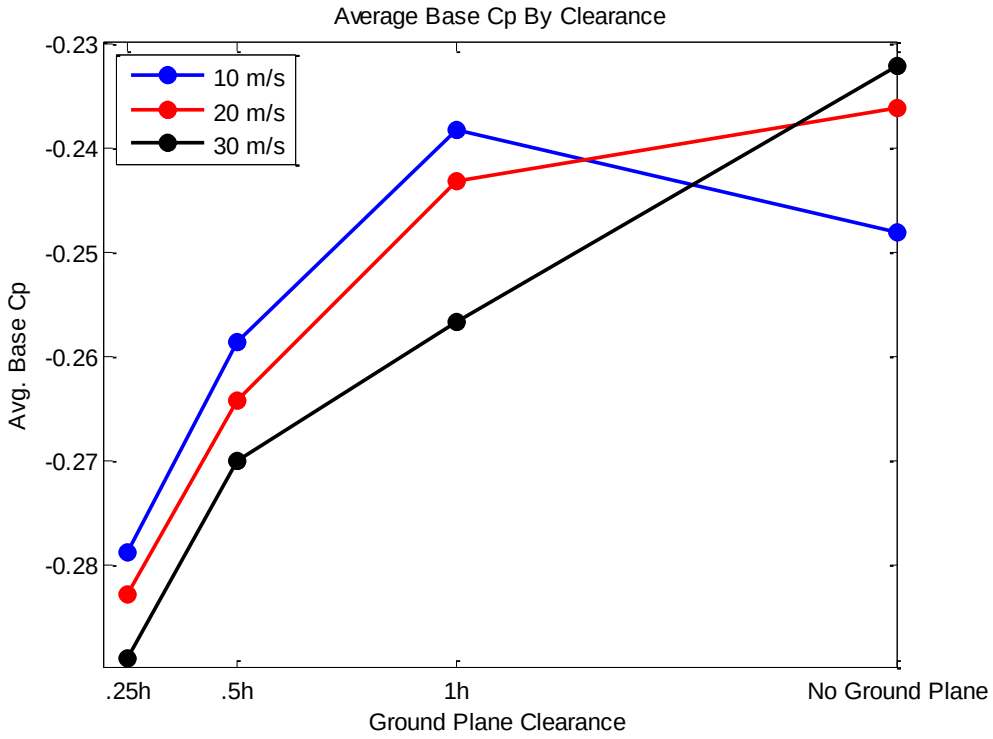

Figure 45: Average Base Pressure for Tabbed Model at Each Ground Clearance

As the model moves closer to the ground plane, the interaction of the ground plane boundary layer, along with the model boundary layer, creates an under body blockage, slowing down the flow. As a result, a low speed jet emerges from the trailing edge gap and creates a much weaker vortex. On the opposite, unbounded flow side, the shear layer is much stronger. This leads to a stronger vortex in comparison to the vortex formed on the bounded side, resulting in a lower pressure dip. This scenario is in agreement with data from Gurlek et al.'s[16]. Gurlek et. al. used PIV to study and analyze the flow field around a tractor trailer over a stationary ground plane. Figure 46 shows the flow

visualization of their experiment. In this figure, it can be seen that there is a tight base vortex on the bottom side of the bluff body that emerges from the gap flow under the body.

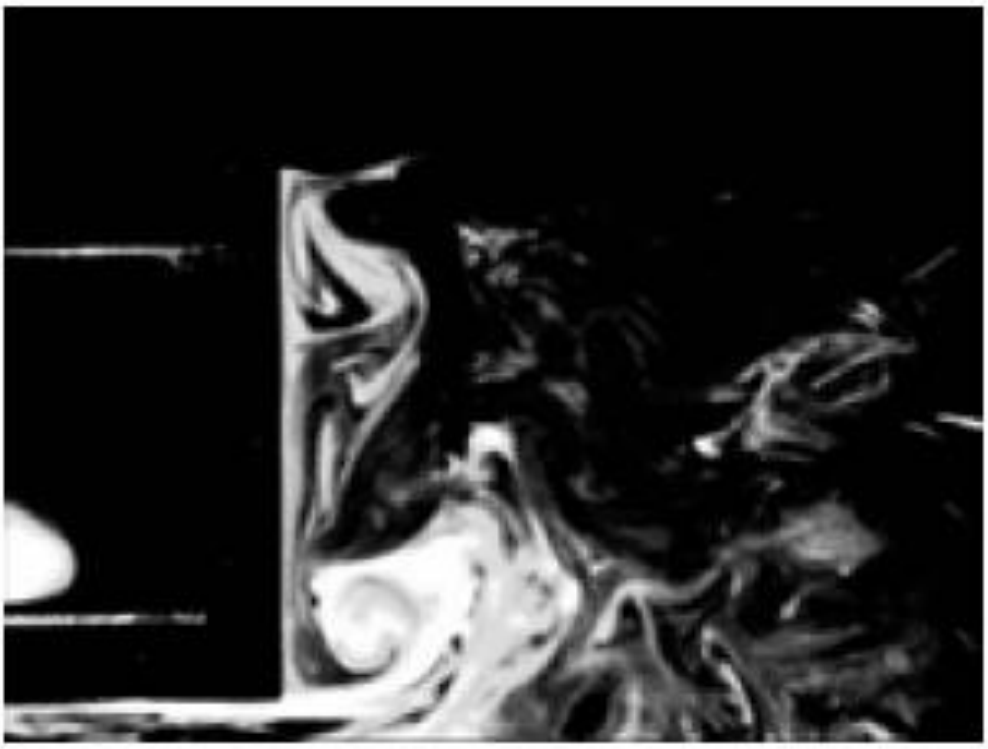

Figure 46: Flow Visualization of the Wake Region for Bluff Body in Ground Effect

Additionally, Gurlek et. al. present velocity profiles in both the normal and spanwise symmetry plane behind their bluff body. It was shown that in the spanwise direction, there is an area of reverse flow in the middle of the base, while the edges saw flow closer to freestream velocity, indicating the formation of equal vortices on each edge. In the normal direction, Gurlek showed that the bounded flow side saw velocities that were much smaller compared to the unbounded flow side, indicating a stronger vortex on the upper, unbounded surface. Overall, results from Gurlek et. al. are similar to flow characteristics presented in this thesis. The introduction of a ground plane created a

higher pressure on the bounded flow side, resulting in a weak vortex region. On the upper surface, the higher momentum shear layer dominates, resulting in a longer, stronger vortex further downstream, and lower pressures on the upper half of the model baseplate.

9. CONCLUSIONS

A bluff body was tested in the proximity of a stationary ground plane in order to show a relationship between base pressure and drag with variations in ground clearance. Initial testing focused on analyzing drag characteristics utilizing trailing edge tabs perpendicular to the free stream flow, and comparing those results seen with the body with no ground effect to previous tests done by Barker. In free stream flow, no drag reduction was found by disturbing the vortex with trailing edge tabs, and a significant increase in drag was found for all test speeds with the inclusion of the tabs, via both base pressure and sting balance force results. Further testing aimed to investigate the effect a stationary ground plane had on the flow properties around a bluff body, with the ground plane intended to mimic real world bounded flow conditions. Three tests were done at speeds of 10, 20 and 30 m/s, with ground plane clearances of 0.25h, 0.50h, and 1h tested at each speed, as well as a baseline case in which the model was tested with no ground plane in the tunnel. Overall, the conclusions from the experiment are as follows:

1) Trailing edge devices are ineffective at attenuating vortex shedding and decreasing overall drag for Reynolds numbers tested between $1.9e^5$ and $5.9e^5$. Sting balance data shows an average increase in drag coefficient of 0.086 for the tabbed model versus the non-tabbed model. Additionally, base pressure readings indicate lower pressure coefficients for the tabbed model compared to the non-tabbed model.

2) The addition of a ground plane decreases overall base pressure coefficients. Compared to the no ground plane present test case, at all Reynolds numbers tested, and all ground clearances, the average base pressure coefficient decreased. Normal base

pressure coefficient profiles that indicated that the presence of a ground plane decreases the pressure on the unbounded flow side of the bluff body, with slight a slight increase in pressure coefficient on the bounded side.

3) Overall base pressure is lowest at the lowest ground clearance of H/h = 0.25, and rises with increasing ground clearance. At the lower ground clearances, the wake region is dominated by the vortex emanating from the unbounded flow side. On the bounded flow side, the low speed, jet-like flow created by the interaction between the stationary ground plane and the underside of the test model likely forms a weak vortex closer to the tailing blunt base.

4) The critical gap height was found to be between H/h = 0.25 and H/h = 0.50, likely influenced by the stationary ground plane. Drag readings show a decrease in drag coefficient from the no ground plane to the H/h = 0.50 test cases, from 0.40 to 0.37, respectively. However, as the ground clearance is lowered from 0.5h to 0.25h the recorded drag coefficient increases, to a C_d of 0.40 at the lowest Reynolds number. This suggests a critical gap height, below which the growth of the stationary ground plane boundary layer begins to affect results.

It is suggested that future testing on bounded flow around a bluff body be undertaken using more accurate techniques, with a moving ground plane as the most accurate choice to model ground vehicle and road interaction. Additionally, the orientation and placement of trailing edge tabs should be re-examined, with special attention paid to the angle at which the trailing edge tabs lie in relation to the flow. In this test, all tabs were perpendicular to the flow, leading to an increase in drag. However,

trailing edge tabular devices that are parallel, or slightly angled from the flow direction should be examined. Lastly, it has been shown that while base pressure drag is the largest contributor to overall drag for a ground vehicle, there are other factors that play a role in overall aerodynamic drag, such as tractor-trailer body gaps and wheel-well interactions for large transport vehicles. Future testing could examine whole vehicle flow properties, with the focus being on a synergistic solution to decreasing overall aerodynamic drag experienced by a moving ground vehicle.

REFERENCES

1 Ahmed, M.R., and Sharma, S.D., "An Investigation on the Aerodynamics of a Symmetrical Airfoil in Ground Effect," *Experimental Thermal and Fluid Science,* Vol. 29, 2005, pp 633-647.

2 Cole, William, "The Pelican: A Big Bird for the Long Haul", *Boeing Frontiers Online,*URL: http://www.boeing.com/news/frontiers/archive/2002/september/i_pw.html [cited 3 Dec 2014].

3 Halloran, M., and O'Meara, S., *Wing in Ground Effect Craft Review.* Royal Melbourne Institute of Technology, 1999.

4 Park, H., Lee, D., Jeon, W-P., Hahn, S., and Kim, J. "Drag Reduction in Flow Over a Two Dimenisonal Bluff Body with a Blunt Trailing Edge Using a New Passive Device," *The Journal of Fluid Mechanics.* 2005, pp 389-414.

5 Pinn, Jarred. *Effect of End-Plate Tabs on Drag Reduction of a 3D Bluff Body with a Blunt Base*. California Polytechnic State University San Luis Obispo, 2012.

6 Erlhoff, Ethan. *Distributed Forcing on A 3D Bluff Body With A Blunt Base An Experimental Active Drag Control Approach*. California Polytechnic State University San Luis Obispo, 2012.

7 Barker, Brian. *Effect of Adaptive Tabs on Drag of a Square-Base Bluff Body.* California Polytechnic State University San Luis Obispo, 2014.

8 Kim, M.S., and Geropp, D., "Experimental Investigation of the Ground Effect on the Flow Around Some Two-Dimensional Bluff Bodies with Moving Belt Technique," *Journal of Wind Engineering and Indstrial Aerodynamics,* Vol. 74-76, 1998, pp 511-519.

9 Fago, B., Lindner, H., Mahrenholtz, O., "The Effect of Ground Simulation on the Flow Around Vehicles in Wind Tunnel Testing," *Journa of Wind Engineering and Industrial Aerodynamics,* Vol. 38, 1991, pp 47-57.

10 Garry, Kevin P., "Some Effects of Ground Clearance and Ground Plane Boundary Layer Thickness on the Mean Base Pressure of a Bluff Vehicle Body Type," *Journal of Wind Engineering and Industrial Aerodynamics,* Volume 62, 1996, pp 1-20.

11 Kim, T. Y., Lee, B., Ku, Y., Lee, D., and Kohama, Y., "The Enhancement of Aerodynamic Characteristics on Bluff Bodies near a Moving Ground," *JSME International Journal,* Series B., Vol. 49, No. 3, 2006, pp 787-796.

12 Patten, J., McAuliffe, B., Mayda, W., and Tanguay, B., "Review of Aerodynamic Drag Reduction Devices for Heavy Trucks and Buses," National Research Council Canada, Project 54-A3578, May 2012.

13 Leuschen, J. and Cooper, K., "Full-Scale Wind Tunnel Tests of Production and Prototype, Second-Generation Aerodynamic Drag-Reducing Devices for Tractor-Trailers," SAE Technical Paper 2006-01-3456, 2006.

14 Bearman, P.W., "Review-Bluff Body Flows Applicable to Vehicle Aerodynamics," *Journal of Fluids Engineering,* Vol. 102, 1980, pp 265-274.

15 Maskell, E.C., "A Theory of the Blockage Effects on Bluff Bodies and Stalled Wings in a Closed Wind Tunnel," R&M 3400, Nov., 1963.

16 Gurlek, C., Sahin, B., Ozalp, C., and Akilli, H., "Flow Structures Around a Thee-Dimensional Rectangular Body with Ground Effect," *Wind and Structures,* Vol. 11, No. 5, 2008, pp 345-359.

17 Taylor, John R., *An Introduction to Error AnalysisL The Study of Uncertainties in Physical Measurements*. University Science Books, 1997.

18 Innes, Paul D., and Carlson, Charles E., "Test and Verification of Vortex Shedding for a 3D Bluff Body,", *California Polytechnic State Univeristy,* 2011.

19 Shi, Liu L., Liu, Ying Z., and Sung, Hyung S., "On the Wake With and Without Vortex Shedding Suppression Behind a Two-Dimensional Square Cylinder in Proximity to a Plane Wall," *Journal of Wind Engineering and Industrial Aerodynamics,* Vol. 98, 2010, pp 492-503.

20 Cai, J., Chng, Tat L., and Tsai Her M.,"On Vortical Flows Shedding from a Bluff Body with a Wavy Trailing Edge," *Physics of Fluids*, Vol. 20, 2008.

21 Straatman, Anthony G., and Martinuzzi, Robert J.,"An Examination of the Effect of Boundary Layer Thickness on Vortex SHedding From a Square Cylinder Near a Wall," Journal of Wind Engineering and Industrial Aerodynamics, Vol. 91, 2003, pp 1023-1037.

22 Hybrid Electrical Vehicle Team, SDSU. "Vehicle Aerodynamics", *College of Engineering, SDSU,* URL: http://engineering.sdsu.edu/~hev/aerodyn.html [cited 14 Jan 2015].

APPENDICES

A: Data Analysis

```
clc
clear all
close all
format long
%%
tabs='No Tabs';

folder_name=uigetdir;
currdir=cd;
cd(folder_name)
tic
files=dir('*.dat');
for i=1:length(files);
    load(files(i).name);

end

Half_h_10mps=Half_h_10mps(2:end);
Half_h_20mps=Half_h_20mps(2:end);
Half_h_30mps=Half_h_30mps(2:end);
No_plane_10mps=No_plane_10mps(2:end);
No_plane_20mps=No_plane_20mps(2:end);
No_plane_30mps=No_plane_30mps(2:end);
One_h_10mps=One_h_10mps(2:end);
One_h_20mps=One_h_20mps(2:end);
One_h_30mps=One_h_30mps(2:end);
Quart_h_10mps=Quart_h_10mps(2:end);
Quart_h_20mps=Quart_h_20mps(2:end);
Quart_h_30mps=Quart_h_30mps(2:end);

num_frames=Half_h_10mps(end-3);
num_ports=Half_h_10mps(end-1);
num_ports=32;

k=0;
data=zeros(12,length(Half_h_10mps)/4);
for i=4:4:length(Half_h_10mps)
    k=k+1;
data(7,k)=Half_h_10mps(i);
data(8,k)=Half_h_20mps(i);
data(9,k)=Half_h_30mps(i);
data(1,k)=No_plane_10mps(i);
data(2,k)=No_plane_20mps(i);
data(3,k)=No_plane_30mps(i);
data(4,k)=One_h_10mps(i);
data(5,k)=One_h_20mps(i);
data(6,k)=One_h_30mps(i);
data(10,k)=Quart_h_10mps(i);
data(11,k)=Quart_h_20mps(i);
```

```
data(12,k)=Quart_h_30mps(i);
end

std_data=zeros(12,num_ports);
psi=zeros(12,num_ports);
for i=1:num_ports
    std_data(1,i)=std(data(1,i:num_ports:end));
    std_data(2,i)=std(data(1,i:num_ports:end));
    std_data(3,i)=std(data(1,i:num_ports:end));
    std_data(4,i)=std(data(1,i:num_ports:end));
    std_data(5,i)=std(data(1,i:num_ports:end));
    std_data(6,i)=std(data(1,i:num_ports:end));
    std_data(7,i)=std(data(1,i:num_ports:end));
    std_data(8,i)=std(data(1,i:num_ports:end));
    std_data(9,i)=std(data(1,i:num_ports:end));
    std_data(10,i)=std(data(1,i:num_ports:end));
    std_data(11,i)=std(data(1,i:num_ports:end));
    std_data(12,i)=std(data(1,i:num_ports:end));

psi(1,i)=mean(data(1,i:num_ports:end));
psi(2,i)=mean(data(2,i:num_ports:end));
psi(3,i)=mean(data(3,i:num_ports:end));
psi(4,i)=mean(data(4,i:num_ports:end));
psi(5,i)=mean(data(5,i:num_ports:end));
psi(6,i)=mean(data(6,i:num_ports:end));
psi(7,i)=mean(data(7,i:num_ports:end));
psi(8,i)=mean(data(8,i:num_ports:end));
psi(9,i)=mean(data(9,i:num_ports:end));
psi(10,i)=mean(data(10,i:num_ports:end));
psi(11,i)=mean(data(11,i:num_ports:end));
psi(12,i)=mean(data(12,i:num_ports:end));
end

CP(1,:)=(psi(1,:)-psi(1,end))/(psi(1,end-1)-psi(1,end));
CP(2,:)=(psi(2,:)-psi(2,end))/(psi(2,end-1)-psi(2,end));
CP(3,:)=(psi(3,:)-psi(3,end))/(psi(3,end-1)-psi(3,end));
CP(4,:)=(psi(4,:)-psi(4,end))/(psi(4,end-1)-psi(4,end));
CP(5,:)=(psi(5,:)-psi(5,end))/(psi(5,end-1)-psi(5,end));
CP(6,:)=(psi(6,:)-psi(6,end))/(psi(6,end-1)-psi(6,end));
CP(7,:)=(psi(7,:)-psi(7,end))/(psi(7,end-1)-psi(7,end));
CP(8,:)=(psi(8,:)-psi(8,end))/(psi(8,end-1)-psi(8,end));
CP(9,:)=(psi(9,:)-psi(9,end))/(psi(9,end-1)-psi(9,end));
CP(10,:)=(psi(10,:)-psi(10,end))/(psi(10,end-1)-psi(10,end));
CP(11,:)=(psi(11,:)-psi(11,end))/(psi(11,end-1)-psi(11,end));
CP(12,:)=(psi(12,:)-psi(12,end))/(psi(12,end-1)-psi(12,end));


for i=1:12
upper_error(i,:)=sqrt(std_data(i,1:num_ports-2).^2+std_data(i,end)^2);
lower_error(i,:)=sqrt(std_data(i,end-1)^2+std_data(i,end)^2);
error(i,:)=(abs(upper_error(i,:)./(psi(i,1:num_ports-2)-psi(i,end)))...
    +abs(lower_error(i,:)/(psi(i,end-1)-
psi(i,end)))).*CP(i,1:num_ports-2);
end

for i=1:12
```

```
    avg_base_CP(i)=mean(CP(i,1:end-2));
end

X_vert=1:1:17;
X_horz=18:1:29;

%creates locations of ports (can be location or port numbers)
x=fliplr([4.875 4.75 4.5 4.25 4 3.5 3 2.5 2 1.5 1 .75 .5 .25 .125]);
%(0,0) at bottom left corner as mounted
x=x-2.5; %sets (0,0) to center of model
x=x/5;
clearance=[.25 .5 1 2];
spanwise_distance=x;
normal_distance=x;

%% Spanwise Graphs
s=figure(1)
errorbar(spanwise_distance,CP(1,16:30),error(1,16:30),'b','marker','x',
'markersize',5,'MarkerFaceColor','b','linewidth',2)
hold on
errorbar(spanwise_distance,CP(4,16:30),error(4,16:30),'k','marker','^',
'markersize',5,'MarkerFaceColor','k','linewidth',2)
errorbar(spanwise_distance,CP(7,16:30),error(7,16:30),'r','marker','v',
'markersize',5,'MarkerFaceColor','r','linewidth',2)
errorbar(spanwise_distance,CP(10,16:30),error(10,16:30),'g','marker','o
','markersize',5,'MarkerFaceColor','g','linewidth',2)
legend('No Ground
Plane','h/H=1','h/H=.5','h/H=.25','location','southwest')
title ('Normal Side Tabs: Spanwise 10 m/s')
axis([-.5 .5 -.55 -.1])
xlabel('z/H')
ylabel('Cp')

figure(2)
errorbar(spanwise_distance,CP(2,16:30),error(2,16:30),'b','marker','x',
'markersize',5,'MarkerFaceColor','b','linewidth',2)
hold on
errorbar(spanwise_distance,CP(5,16:30),error(5,16:30),'k','marker','^',
'markersize',5,'MarkerFaceColor','k','linewidth',2)
errorbar(spanwise_distance,CP(8,16:30),error(8,16:30),'r','marker','v',
'markersize',5,'MarkerFaceColor','r','linewidth',2)
errorbar(spanwise_distance,CP(11,16:30),error(11,16:30),'g','marker','o
','markersize',5,'MarkerFaceColor','g','linewidth',2)
legend('No Ground
Plane','h/H=1','h/H=.5','h/H=.25','location','southwest')
title('Normal Side Tabs: Spanwise 20 m/s')
axis([-.5 .5 -.55 -.1])
xlabel('z/H')
ylabel('Cp')


figure(3)
errorbar(spanwise_distance,CP(3,16:30),error(3,16:30),'b','marker','x',
'markersize',5,'MarkerFaceColor','b','linewidth',2)
hold on
```

```
errorbar(spanwise_distance,CP(6,16:30),error(6,16:30),'k','marker','^',
'markersize',5,'MarkerFaceColor','k','linewidth',2)
errorbar(spanwise_distance,CP(9,16:30),error(9,16:30),'r','marker','v',
'markersize',5,'MarkerFaceColor','r','linewidth',2)
errorbar(spanwise_distance,CP(12,16:30),error(12,16:30),'g','marker','o
','markersize',5,'MarkerFaceColor','g','linewidth',2)
legend('No Ground
Plane','h/H=1','h/H=.5','h/H=.25','location','southwest')
title('Normal Side Tabs: Spanwise 30 m/s')
axis([-.5 .5 -.55 -.1])
xlabel('z/H')
ylabel('Cp')

%%  Normal Graphs
n=figure(4)
errorbar(normal_distance,horzcat(CP(1,1:7),CP(1,23),CP(1,9:15)),horzcat
(error(1,1:7),error(1,23),error(1,9:15)),'b','marker','x','markersize',
5,'MarkerFaceColor','b','linewidth',2)
hold on
errorbar(normal_distance,horzcat(CP(4,1:7),CP(4,23),CP(4,9:15)),horzcat
(error(4,1:7),error(4,23),error(4,9:15)),'k','marker','^','markersize',
5,'MarkerFaceColor','k','linewidth',2)
errorbar(normal_distance,horzcat(CP(7,1:7),CP(7,23),CP(7,9:15)),horzcat
(error(7,1:7),error(7,23),error(7,9:15)),'r','marker','v','markersize',
5,'MarkerFaceColor','r','linewidth',2)
errorbar(normal_distance,horzcat(CP(10,1:7),CP(10,23),CP(10,9:15)),horz
cat(error(10,1:7),error(10,23),error(10,9:15)),'g','marker','o','marker
size',5,'MarkerFaceColor','g','linewidth',2)
legend('No Ground
Plane','h/H=1','h/H=.5','h/H=.25','location','southwest')
title ('Normal Side Tabs: Normal 10 m/s')
axis([-.5 .5 -.55 -.1])
xlabel('y/H')
ylabel('Cp')

figure(5)
errorbar(normal_distance,horzcat(CP(2,1:7),CP(2,23),CP(2,9:15)),horzcat
(error(2,1:7),error(2,23),error(2,9:15)),'b','marker','x','markersize',
5,'MarkerFaceColor','b','linewidth',2)
hold on
errorbar(normal_distance,horzcat(CP(5,1:7),CP(5,23),CP(5,9:15)),horzcat
(error(5,1:7),error(5,23),error(5,9:15)),'k','marker','^','markersize',
5,'MarkerFaceColor','k','linewidth',2)
errorbar(normal_distance,horzcat(CP(8,1:7),CP(8,23),CP(8,9:15)),horzcat
(error(8,1:7),error(8,23),error(8,9:15)),'r','marker','v','markersize',
5,'MarkerFaceColor','r','linewidth',2)
errorbar(normal_distance,horzcat(CP(11,1:7),CP(11,23),CP(11,9:15)),horz
cat(error(11,1:7),error(11,23),error(11,9:15)),'g','marker','o','marker
size',5,'MarkerFaceColor','g','linewidth',2)
legend('No Ground
Plane','h/H=1','h/H=.5','h/H=.25','location','southwest')
title ('Normal Side Tabs: Normal 20 m/s')
axis([-.5 .5 -.55 -.1])
xlabel('y/H')
ylabel('Cp')
```

```
figure(6)
errorbar(normal_distance,horzcat(CP(3,1:7),CP(3,23),CP(3,9:15)),horzcat
(error(3,1:7),error(3,23),error(3,9:15)),'b','marker','x','markersize',
5,'MarkerFaceColor','b','linewidth',2)
hold on
errorbar(normal_distance,horzcat(CP(6,1:7),CP(4,23),CP(6,9:15)),horzcat
(error(6,1:7),error(6,23),error(6,9:15)),'k','marker','^','markersize',
5,'MarkerFaceColor','k','linewidth',2)
errorbar(normal_distance,horzcat(CP(9,1:7),CP(7,23),CP(9,9:15)),horzcat
(error(9,1:7),error(9,23),error(9,9:15)),'r','marker','v','markersize',
5,'MarkerFaceColor','r','linewidth',2)
errorbar(normal_distance,horzcat(CP(12,1:7),CP(10,23),CP(12,9:15)),horz
cat(error(12,1:7),error(12,23),error(12,9:15)),'g','marker','o','marker
size',5,'MarkerFaceColor','g','linewidth',2)
legend('No Ground
Plane','h/H=1','h/H=.5','h/H=.25','location','southwest')
title ('Normal Side Tabs: Normal 30 m/s')
axis([-.5 .5 -.55 -.1])
xlabel('y/H')
ylabel('Cp')

figure(7)
plot(clearance,fliplr(avg_base_CP(1:3:12)),'k','marker','o','MarkerFace
Color','k','linewidth',2)
hold on
plot(clearance,fliplr(avg_base_CP(2:3:12)),'r','marker','o','MarkerFace
Color','r','linewidth',2)
plot(clearance,fliplr(avg_base_CP(3:3:12)),'b','marker','o','MarkerFace
Color','b','linewidth',2)
set(gca,'xtick',[.25 .5 1 2])
set(gca,'xticklabel',{'.25h','.5h','1h','No Ground Plane'})
legend('10 m/s','20 m/s','30 m/s','location','northwest')
xlabel('Ground Plane Clearance')
ylabel('Avg. Base Cp')
title('Average Base Cp By Clearance')

CP(:,8)=CP(:,23);
figure(12)
  subplot(2,2,1)

plot(spanwise_distance,CP(1,16:30),'k','marker','o','MarkerFaceColor','
k','markersize',3)
  hold on
plot(spanwise_distance,CP(2,16:30),'r','marker','o','MarkerFaceColor','
r','markersize',3)
plot(spanwise_distance,CP(3,16:30),'b','marker','o','MarkerFaceColor','
b','markersize',3)
  legend('10 m/s','20 m/s','30 m/s','location','se')
  axis([-.5 .5 -.45 -.1])
  ylabel('C_p')
  xlabel('z/h')
  title('No Ground Plane')
  subplot(2,2,2)
plot(spanwise_distance,CP(4,16:30),'k','marker','o','MarkerFaceColor','
k','markersize',3)
```

```
  hold on
plot(spanwise_distance,CP(5,16:30),'r','marker','o','MarkerFaceColor','
r','markersize',3)
plot(spanwise_distance,CP(6,16:30),'b','marker','o','MarkerFaceColor','
b','markersize',3)
  axis([-.5 .5 -.45 -.1])
   ylabel('C_p')
  xlabel('z/h')
  title('Ground Clearance: H/H=1')
  subplot(2,2,3)
plot(spanwise_distance,CP(7,16:30),'k','marker','o','MarkerFaceColor','
k','markersize',3)
  hold on
plot(spanwise_distance,CP(8,16:30),'r','marker','o','MarkerFaceColor','
r','markersize',3)
plot(spanwise_distance,CP(9,16:30),'b','marker','o','MarkerFaceColor','
b','markersize',3)
  axis([-.5 .5 -.45 -.1])
   ylabel('C_p')
  xlabel('z/h')
  title('Ground Clearance: H/H=0.5')
  subplot(2,2,4)
plot(spanwise_distance,CP(10,16:30),'k','marker','o','MarkerFaceColor',
'k','markersize',3)
  hold on
plot(spanwise_distance,CP(11,16:30),'r','marker','o','MarkerFaceColor',
'r','markersize',3)
plot(spanwise_distance,CP(12,16:30),'b','marker','o','MarkerFaceColor',
'b','markersize',3)
  axis([-.5 .5 -.45 -.1])
   ylabel('C_p')
  xlabel('z/h')
  title('Ground Clearance: H/H=0.25')


figure(13)
subplot(2,2,1)
plot(spanwise_distance,CP(1,1:15),'k','marker','o','MarkerFaceColor','k
','markersize',3)
  hold on
plot(spanwise_distance,CP(2,1:15),'r','marker','o','MarkerFaceColor','r
','markersize',3)
plot(spanwise_distance,CP(3,1:15),'b','marker','o','MarkerFaceColor','b
','markersize',3)
  legend('10 m/s','20 m/s','30 m/s','location','se')
  axis([-.5 .5 -.45 -.1])
  ylabel('C_p')
  xlabel('y/h')
  title('No Ground Plane')
  subplot(2,2,2)
plot(spanwise_distance,CP(4,1:15),'k','marker','o','MarkerFaceColor','k
','markersize',3)
hold on
plot(spanwise_distance,CP(5,1:15),'r','marker','o','MarkerFaceColor','r
','markersize',3)
```

```
plot(spanwise_distance,CP(6,1:15),'b','marker','o','MarkerFaceColor','b
','markersize',3)
  axis([-.5 .5 -.45 -.1])
   ylabel('C_p')
  xlabel('y/h')
  title('Ground Clearance: H/H=1')
  subplot(2,2,3)
plot(spanwise_distance,CP(7,1:15),'k','marker','o','MarkerFaceColor','k
','markersize',3)
  hold on
plot(spanwise_distance,CP(8,1:15),'r','marker','o','MarkerFaceColor','r
','markersize',3)
plot(spanwise_distance,CP(9,1:15),'b','marker','o','MarkerFaceColor','b
','markersize',3)
  axis([-.5 .5 -.45 -.1])
   ylabel('C_p')
  xlabel('y/h')
  title('Ground Clearance: H/H=0.5')
  subplot(2,2,4)
plot(spanwise_distance,CP(10,1:15),'k','marker','o','MarkerFaceColor','
k','markersize',3)
  hold on
plot(spanwise_distance,CP(11,1:15),'r','marker','o','MarkerFaceColor','
r','markersize',3)
plot(spanwise_distance,CP(12,1:15),'b','marker','o','MarkerFaceColor','
b','markersize',3)
  axis([-.5 .5 -.45 -.1])
   ylabel('C_p')
  xlabel('y/h')
  title('Ground Clearance: H/H=0.25')
```

$$C_P = \frac{P - P_\infty}{q_\infty} = \frac{P - P_\infty}{P_t - P_\infty}$$

$$\frac{dC_P}{C_P} = \frac{d(P - P_\infty)}{P - P_\infty} - \frac{d(P_t - P_\infty)}{P_t - P_\infty} = \frac{dP}{P - P_\infty} - \frac{dP_\infty}{P - P_\infty} - \frac{dP_t}{P_t - P_\infty} + \frac{dP_\infty}{P_t - P_\infty}$$

$$\frac{dC_P}{C_P} \approx \frac{dP}{P - P_\infty} + \left(\frac{-1}{P - P_\infty} + \frac{1}{P_t - P_\infty}\right) dP_\infty - \frac{dP_t}{P_t - P_\infty}$$

So

$$\sigma_{C_P} \approx |C_P| \sqrt{\left(\frac{\sigma_P}{P - P_\infty}\right)^2 + \left[\left(\frac{-1}{P - P_\infty} + \frac{1}{P_t - P_\infty}\right)\sigma_{P_\infty}\right]^2 + \left(\frac{\sigma_{P_t}}{P_t - P_\infty}\right)^2}$$

$$C_P = \frac{P - P_\infty}{P_t - P_\infty} = \frac{-0.0997 - (-0.0840)}{-0.0055 - (-0.0840)} = -0.2000$$

$$\sigma_{C_P} \approx |-0.2000| \sqrt{\left(\frac{.0012}{-0.0977 - (-0.0840)}\right)^2 + \left[\left(\frac{-1}{-0.0977 - 0.0840} + \frac{1}{-0.0055 - 0.0840}\right) 2.4649 * 10^{-4}\right]^2 + \cdots \cdots \left(\frac{1.0449 * 10^{-4}}{-0.0055 - 0.0840}\right)^2}$$

$$\boldsymbol{\sigma_{C_P} \approx 0.0016}$$

$$C_D = \frac{D}{q_\infty A} = \frac{D}{(P_t - P_\infty)A}$$

$$\frac{dC_D}{C_D} = \frac{dD}{D} - \frac{d(P_t - P_\infty)}{P_t - P_\infty} - \frac{dA}{A} = \frac{dD}{D} - \frac{dP_t}{P_t - P_\infty} + \frac{dP_\infty}{P_t - P_\infty} - \frac{dA}{A}$$

Neglect A, so

$$\frac{dC_D}{C_D} \approx \frac{dD}{D} - \frac{dP_t}{P_t - P_\infty} + \frac{dP_\infty}{P_t - P_\infty}$$

So

$$\sigma_{C_D} \approx |C_D| \sqrt{\left(\frac{\sigma_D}{D}\right)^2 + \left(\frac{\sigma_{P_t}}{P_t - P_\infty}\right)^2 + \left(\frac{\sigma_{P_\infty}}{P_t - P_\infty}\right)^2}$$

$$C_D = \frac{D}{q_\infty * S} = \frac{0.3959}{4.9488 * \ 0.1736} = 0.4612$$

$$\sigma_{C_D} \approx |0.4612| \sqrt{\left(\frac{0.013}{0.3959}\right)^2 + \left(\frac{1.0449 * 10^{-4}}{-0.0055 - 0.0840}\right)^2 + \left(\frac{2.649 * 10^{-4}}{-0.0055 - 0.0840}\right)^2}$$
$$\approx 0.0162$$

$$\boldsymbol{\sigma_{C_D} \approx 0.015}$$

B: Supporting Literature Review Data

Graphs from Gurlek et. al.[15]

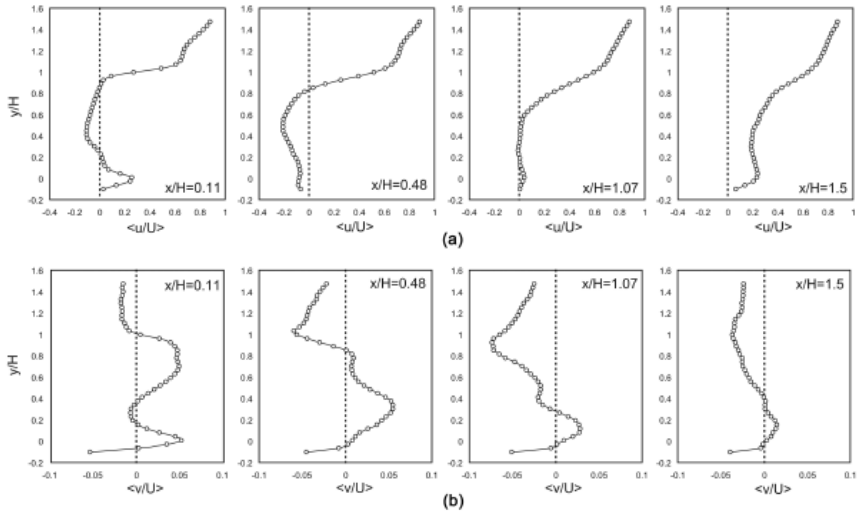

Fig. 3 Velocity profiles of the flow in the vertical symmetry plane in the wake region. (a) Dimensionless streamwise velocity component, <*u*/*U*>, (b) Dimensionless spanwise velocity component, <*v*/*U*>.

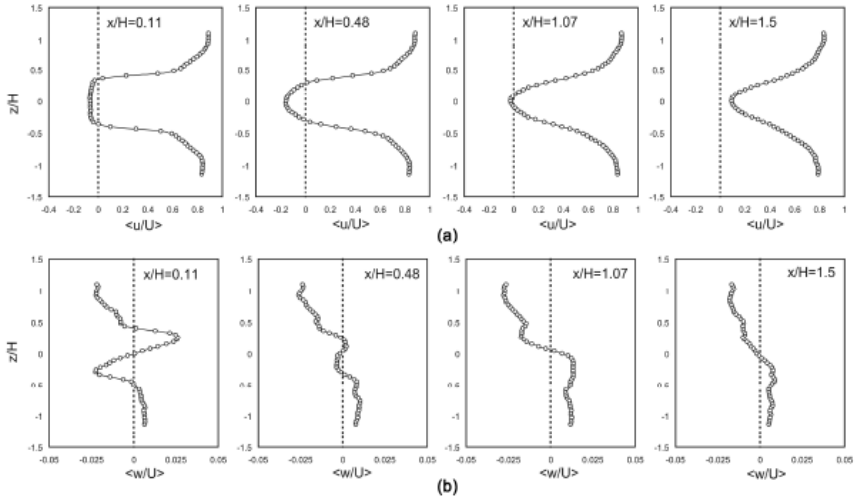

Fig. 6 Velocity profiles of the flow in the horizontal symmetry plane in the wake region. (a) Dimensionless streamwise velocity component, <*u*/*U*>, (b) Dimensionless spanwise velocity component, <*w*/*U*>.

Graphs from Bearman[14]

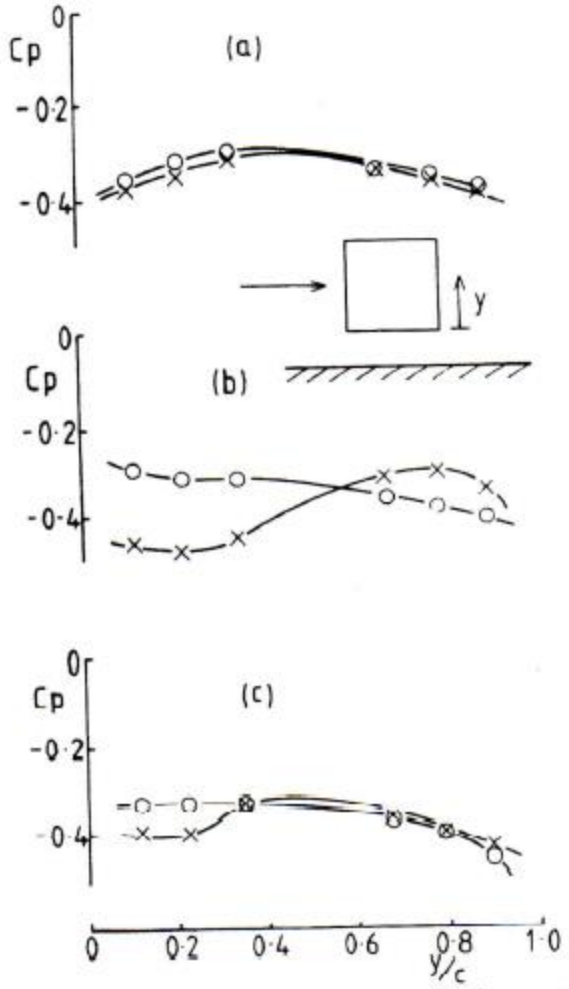

Fig. 5 Base pressure distribution on a cube; X, stationary ground; 0, moving ground. *(a)* $e/c = 1.0$, *(b)* $e/\delta = 0.11$, *(c)* $e/c = 0.056$.